Interplay between effects of barrier tilting and scatterers within a barrier on tunneling transport of Dirac electrons in graphene

Farhana Anwar, Andrii Iurov, Danhong Huang, Godfrey Gumbs, and Ashwani Sharma

Phys. Rev. B **101**, 115424 — Published 23 March 2020

DOI: 10.1103/PhysRevB.101.115424

Interplay between effects of barrier tilting and scatterers within a barrier on tunneling transport of Dirac electrons in graphene

Farhana Anwar[1,2*], Andrii Iurov[3,1†], Danhong Huang[4], Godfrey Gumbs[5,6] and Ashwani Sharma[1,2,4]
[1] *Center for High Technology Materials, University of New Mexico, 1313 Goddard SE, Albuquerque, NM 87106, USA*
[2] *Department of Electrical and Computer Engineering, University of New Mexico, Albuquerque, NM 87106, USA*
[3] *Department of Physics and Computer Science, Medgar Evers College of City University of New York, Brooklyn, NY 11225, USA*
[4] *Air Force Research Laboratory, Space Vehicles Directorate, Kirtland Air Force Base, NM 87117, USA*
[5] *Department of Physics and Astronomy, Hunter College of the City University of New York, 695 Park Avenue, New York, NY 10065, USA*
[6] *Donostia International Physics Center (DIPC), P de Manuel Lardizabal, 4, 20018 San Sebastian, Basque Country, Spain*
(Dated: March 5, 2020)

Dirac-electronic tunneling and transport properties with both finite and zero energy bandgap are investigated for graphene with an in-plane tilted potential barrier embedded with scatters. For a tilted barrier, by using Wentzel-Kramers-Brillouin approximation, an analytical solution is obtained first for transmission coefficient of Dirac electrons in gapped graphene in the absence of any scatters. In the presence of either a single or a continuous distribution of scatters embedded within a tilted barrier, however, a numerical scheme based on finite-difference approach is developed for accurately calculating both transmission coefficient and tunneling resistance of Dirac electrons. Here, the combination of a tilted barrier and a scatter potential can be viewed as an effective barrier-potential profile facilitated by a proper gate structure. Meanwhile, a full analysis and detailed comparisons are presented for the interplay between effects of both distributed scatters in a barrier and barrier tilting on tunneling transport of Dirac electrons in graphene. The barrier-tilting field and scatter position are found to play a key role in controlling a peak of tunneling resistance as well as in its switching to a cusp by a mid-barrier-embedded scatter as the incident energy reaches the Dirac point in a barrier. Different from a single scatter, a continuous distribution within a barrier can enhance the unimpeded incoherent tunneling for head-on collision while greatly suppresses skew ones with increasing barrier-tilting field. All these predicted attractive transport properties are expected extremely useful for designing both novel electronic and optical graphene-based devices and electronic lenses in ballistic-electron optics.

I. INTRODUCTION

Graphene, a one atom-thick allotrope of carbon, being a conductor with exceptionally large mobility at a large range of ambient temperatures, makes a strong case for a number of ballistic transport nanodevices. It has unique electronic properties due to its linear energy dispersion with zero bandgap, as well as a spinor two-component wave function. These unique characteristics give rise to some highly unusual electronic and transport properties. [1–4]

These peculiar properties result in a fact that a potential barrier becomes transparent to electrons arriving at normal incidence regardless of its height or width. This effect, known as Klein tunneling, [1] restricts the switching-off capability (i.e., complete pinch-off of electric current) for logical applications, and makes graphene difficult to achieve logical functionalities without use of chemical modification or patterning. [5–8]

On the other hand, such a situation also offers a unique possibility to fabricate various ballistic devices and circuits in which electrons experience focusing (i.e., direction filtering) by one or several potential barriers. Practically, a zero-bandgap two-dimensional material acquires an important advantage over metals in its capability to tune the conductivity by means of either chemical doping or a gate voltage for creating an in-plane potential barrier with a desired geometrical pattern. [9–11]

Interestingly, the induced planar barrier structure within a grraphene sheet can be realized by applying a gate voltage. This is quite different from the design of a high-electron-mobility transistor. For example, by using different

* fanwar@unm.edu
† theorist.physics@gmail.com

inhomogeneous profiles of static bias voltage, various band alignments and junction structures, such as bipolar ($p-n$, $n-p$, $p-n-p$, $n-p-n$, etc.) as well as unipolar junctions ($n-n'$, $p-p'$) can be facilitated [12–18] to achieve desired gate-voltage (barrier-height) dependence of electrical conductance. In spite of the considered junction being abrupt or smooth, its angular selectivity for carrier transport makes it a unique one in comparison with conventional semiconductor junctions, e.g., metaloxidesilicon field-effect transistors.

Other significant roles played by our proposed tunable junctions include Veselago lens [19,20] by exploiting optics-like behavior of ballistic Dirac electrons, Fabry-Perot interferometer, [13] subthermal switches, [5] and Andreev reflections [21]. Therefore, in order to design next-generation graphene-based electronics, it is crucial to gain a full understanding of physics mechanism for ballistic transports across various types of potential barriers in graphene. Negative refractive index with a single ballistic graphene junction, which is associated with electron-hole switching, has already been observed experimentally, [5,15] and it strongly affects the operation of an electric switch. [5,22,23]

In connection with related graphene studies, the works by Katsnelson, et al. [24,25] described the Klein paradox, i.e., unimpeded tunneling for a head-on collision through a square potential barrier in graphene, as one of the fundamental properties of any Dirac-cone structure due to its relativistic energy dispersions. In bilayer graphene, however, there exists a high impedance and a full reflection for such types of potential barriers. In addition, the paper by Zalipaev, et al. represented the first attempt to evaluate electron wave function in semi-classical Wentzel-Kramers-Brillouin (WKB) approximation for graphene with a finite energy gap. This results could be applied to studying electron tunneling and finding transmission coefficient for potential barriers with various profiles. [26] Furthermore, the reported research by Reijnders, et al. addressed the optical properties of graphene with an energy gap by using the semi-classical model. [27] Finally, Choubabi, et al. considered a linear potential barrier which oscillates uniformly in time and obtained a solution for the energy spectrum including several modes associated with oscillations. [28]

An investigation on impurity-assisted electron tunneling conductance was reported for a very specific case of undoped, or intrinsic graphene, [29] in which a resonant-type conductance enhancement was found for the case with a single impurity atom. In the presence of one-dimensional fluctuations of a disorder potential, its connection to Anderson localization was further discussed. On the other hand, the defect effect on transport properties was also studied, including one-parameter scaling with respect to sample size [30] and some critical phenomena induced by electron-electron interactions in graphene and topological insulators [31].

Various theoretical models have been adopted aiming to obtain electron transport in graphene, including transfer matrix, [32–34] non-equilibrium Green's function, [6,35] tight-binding model, [36,37] as well as semi-classical WKB approximation [14,17,36]. However, there are still few of studies on electronic transport properties using finite-difference approach [38] (FDA) in numerical calculation for an arbitrary potential profile. A crucial advantage of FDA is a possibility to take into account of a single or multiple and even a continuous distribution of scatters embedded within a barrier. A number of fabricated optical devices face such a situation, which detriments the device performance [8,23] while trying to accomplish ballistic $p-n$ junction characteristics experimentally. Alternatively, some smooth $p-n$ and $n-p-n$ junctions in graphene were realized and analyzed theoretically (see Refs. [7,8,12,13,15,39,40] for details).

From the perspective of newly proposed methodology, the use of FDA introduced in this paper makes it possible to accurately calculate tunneling of Dirac electrons in graphene through a tilted potential barrier in the presence of either a single or a continuous distribution of scatters embedded within a barrier. From the viewpoint of introducing new physics, on the other hand, applying FDA allows ones to exactly analyze effects of barrier tilting as well as of scatters on tunneling of Dirac electrons. More importantly, by taking advantage of our newly developed methodology, the FDA facilitates a direct comparison for the interplay between effects of distributed scatters in a barrier and barrier tilting on tunneling transport of Dirac electrons in graphene, which becomes the main focus of the current paper.

The main goal of our paper is to develop a new technique for calculating wave functions anywhere in the barrier region and beyond it, transmission and reflection coefficient based on the finite-difference numerical solution of the Dirac scattering equation inside the barrier region. This method is extremely powerful and could be applied to any types of potential profiles. Specifically, our method allows to consider electron tunneling in the presence of scatters embedded within a tilted barrier, including single scatter or a continuously-distributed scatters. As an application of this FDA, we have studied the competition between different effects from distributed scatters in a barrier and from barrier tilting for tunneling transport of Dirac electrons in a graphene layer.

The remaining part of this paper is organized as follows. In Sec. II, we present analytical results within the WKB approximation for both large and small tilting-field limits, accompanied by numerical results for transmission coefficient as functions of both incident angles and electron energy. We introduce FDA in Sec. III for calculating transmission coefficient of Dirac electrons in graphene in the presence of a tilted potential barrier embedded with either a single or a continuous distribution of scatters, along with numerical results of transmission coefficient as functions of incident angles, electron energy, scatter positions and strengths, as well as tunneling resistance as a

function incident incident energy, with various values of tilting field, scatter positions and strengths. Finally, our concluding remarks are presented in Sec. IV.

II. TUNNELING THROUGH A TILTED BARRIER IN WKB APPROXIMATION

In this section, we would highlight the physics behind tunneling transport of ballistic Dirac electrons. For this purpose, we will first introduce the Wentzel-Kramers-Brillouin (WKB) approximation so as to analyze explicitly the dynamics of Dirac-electron tunneling.

Let us consider a tilted potential barrier, as shown in Fig. 1, with the potential $V_B(x) = V_0 + \alpha x$, while $V_B(x) = 0$ outside of the barrier region. For this case, the effective $x-$dependent wave number $k(x)$ can be written as

$$k(x) = \frac{\varepsilon - V_B(x)}{\hbar v_F} = \frac{\varepsilon - V_0}{\hbar v_F} - ax \ , \tag{1}$$

where ε is the kinetic energy of an incoming particle, which is conserved for an elastic scattering with the barrier, and $a \equiv \alpha/(\hbar v_F)$. For a square barrier, as considered in Ref. [2], we simply set $a = 0$ and will use it to build up our perturbation theory for a weak tilting field.

For simplification we introduce a unitary transformation for a gapless Dirac Hamiltonian, i.e., a $\pi/2$-rotation around the $x-$axis, as employed in Ref. [14]. This leads to the mixed eigen-function $\Phi(x\,|\,k_y) = [\phi_+,\, \phi_-]^T$, where $\phi_\pm = (\phi_B \pm \phi_A)/\sqrt{2}$. If $V_B(x) \equiv V_0$ for a constant barrier, we find the eigen-function

$$\Psi_0(x,\, y\,|\,k_y) = \begin{bmatrix} \phi_+ \\ \\ \phi_- \end{bmatrix} \mathsf{e}^{ik_y y} = \frac{1}{2} \begin{bmatrix} \mathsf{e}^{i\theta_{\mathbf{k}}} + 1 \\ \\ \mathsf{e}^{i\theta_{\mathbf{k}}} - 1 \end{bmatrix} \mathsf{e}^{ik_x^{(0)} x + ik_y y} \ , \tag{2}$$

where $\theta_{\mathbf{k}} = \tan^{-1}(k_y/k_x^{(0)})$ is the in-plane angle in the momentum space, $k_x^{(0)} = \sqrt{[(1/\hbar v_F)(\varepsilon - V_0)]^2 - k_y^2}$, and the wave-function amplitude is independent of x and y.

In the most general case, the wave-function amplitudes $\psi_\pm(x,\, y)$ satisfy the following equations [14]

$$\mp i \frac{\partial \psi_\pm}{\partial x} \mp \frac{\partial \psi_\mp}{\partial y} = k(x)\, \psi_\pm \ . \tag{3}$$

Throughout our derivation, the translational symmetry in the y direction is kept always since our potential $V_B(x)$ varies only along the $x-$axis. Correspondingly, we write down $\psi_\pm(x,\, y) = \mathsf{exp}(ik_y y)\, \phi_\pm(x)$. This simplify Eq. (3) into

$$\mp i\, \partial_x \phi_\pm(x) \mp i k_y\, \phi_\mp(x) = k(x)\, \phi_\pm(x) \ , \tag{4}$$

where $\partial_x \phi(x) \equiv d\phi(x)/dx$. As a special case, one can easily verify that the solution $\Psi_0(x,\, y\,|\,k_y)$ in Eq. (2) satisfies Eq. (4) as $V_B(x) = V_0$ or $a = 0$ is taken in Eq. (1) for $k(x)$.

A. WKB Semi-Classical Approach

The general form of semi-classical WKB expansion for a tunneling-electron wave function $\Psi(x,\, y\,|\,k_y)$ can be expressed as [26]

$$\Psi(x,\, y\,|\,k_y) = \mathsf{e}^{(i/\hbar)\, S_\Delta(x)} \sum_{s=0}^{\infty} (-i\hbar)^s\, \Psi_s(x,\, y\,|\,k_y) \ , \tag{5}$$

where $S_\Delta(x) = \hbar \int_x d\xi\, k_x(\xi)$ represents an action. Here, we will only consider the leading $s = 0$ term in Eq. (5) and obtain

$$\Psi_{\pm}(x,\, y\,|\,k_y) = \frac{1}{2}\,\mathbb{C}_{\Delta}(x\,|\,k_y)\,\left(\mathsf{e}^{i\Theta_{\Delta}(x\,|\,k_y)} \pm 1\right)\,\mathtt{exp}\left[\frac{i}{\hbar}\,S_{\Delta}(x)\right]\,\mathsf{e}^{ik_y y}\ , \tag{6}$$

where $k_x(\xi) = (1/\hbar v_F)\sqrt{[\varepsilon - V_B(\xi)]^2 - (\hbar v_F k_{\Delta})^2}$, $k_{\Delta} = (1/\hbar v_F)\sqrt{(\hbar v_F k_y)^2 + \Delta_G^2}$ is independent of ξ, and $2\Delta_G$ is the bandgap between the valence and conduction bands. Furthermore, we have also introduced the following two dimensionless quantities in Eq. (6), i.e.,

$$\begin{aligned}
\mathbb{C}_{\Delta}(x\,|\,k_y) &= \frac{1}{k_x(x)}\,\left\{k_{-}(x) + i\,\frac{\Delta_G[\varepsilon - \Delta_G - V_B(x)]}{(\hbar v_F)^2\,k_y}\right\}\ , \\
\Theta_{\Delta}(x\,|\,k_y) &= \tan^{-1}\left[\frac{\hbar v_F\,k_{+}(x)}{\varepsilon - \Delta_G - V_B(x)}\right]\ ,
\end{aligned} \tag{7}$$

where $k_{\pm}(x) = k_x(x) \pm i k_y$. It is straightforward to verify that the above solution reduces to that of gapless graphene with $\Delta_G = 0$, yielding [14]

$$\Psi_{\pm}(x,\, y\,|\,k_y) = \frac{k_{+}(x) \pm k(x)}{2\sqrt{|k(x)|\,k_x(x)}}\,\mathtt{exp}\left[i\int^{x} d\xi\,k_x(\xi)\right]\,\mathsf{e}^{ik_y y}\ . \tag{8}$$

where $k(x)$ has already been defined in Eq. (1).

As an electron moves uphill with increasing potential, the sum of its potential and kinetic energies remains to be a constant. Therefore, the kinetic energy of the electron will decrease on its way. For this situation, we need define a *turning point for a semi-classical trajectory*, at which $k_x(x) = 0$ but the total kinetic energy is still positive due to $k_y \neq 0$. Setting $k(x) = 0$ in Eq. (1), we find the turning point $x_0 = (\varepsilon - V_0)/\alpha$, where a Dirac electron changes into a Dirac hole. Moreover, the range corresponding to $|x - x_0| < \xi_c$ becomes a classically forbidden region in which $k_x(x)$ become imaginary, where $\xi_c = \hbar v_F k_y/\alpha$ for $\Delta_G = 0$. If this forbidden region lies entirely within the tilted-barrier region, the transmission coefficient $T(\alpha\,|\,k_y)$ is found to be [26]

$$T(\alpha\,|\,k_y) \backsim \mathtt{exp}\left[-2\int_{x_0-\xi_c}^{x_0+\xi_c} d\xi\,\sqrt{k_y^2}\right] = \mathtt{exp}\left(-\frac{4k_y^2}{a}\right)\ , \tag{9}$$

which is a clear manifestation of the conservation of the Klein paradox for a tilted-barrier.

For the case with $\Delta_G > 0$, the result in Eq. (9) could be generalized to

$$\begin{aligned}
&T_{\Delta}(\alpha\,|\,k_y) \backsim \mathtt{exp}\left[-2\int_{x_0-\xi_c}^{x_0+\xi_c} d\xi\,\sqrt{k_{\Delta}^2(\xi)}\right] = \mathtt{exp}\left\{-\frac{4}{a}\left[k_y^2 + (\Delta_G/\hbar v_F)^2\right]\right\}\ , \\
&\text{with}\quad \xi_c = \frac{1}{\alpha}\sqrt{(\hbar v_F k_y)^2 + \Delta_G^2}\ .
\end{aligned} \tag{10}$$

Therefore, Klein paradox will not exist for any α and k_y values. In addition, an exact solution for the wave function in this case could also be obtained by using the results in Ref. [14], as shown in Appendix A.

B. Perturbative Solution for Small Tilting

Here, we would like to emphasize that all the results obtained in previous subsection suffer a limitation, i.e., they are valid only if the electron-to-hole switching occurs inside the barrier region. However, this becomes invalid if either the slope α of a potential profile or the barrier width W_B becomes very small.

To seek for a perturbative solution within a barrier, we first assume a very small slope α to ensure $a = \alpha/\hbar v_F \ll k^2(x)$. We further assume $\varepsilon > V_B(x)$ so that particle-hole switching will not occur. As a result, the wave function

takes the form $\psi_{A,B}(x,y) = \phi_{A,B}(x)\,\mathtt{exp}(ik_y y)$ and Eq. (4) can be applied to find solution for $\phi_{A,B}(x)$. In this case, however, a $\pi/2$-rotation for $\phi_{\pm}(x)$ is not needed.

For $V_B(x) = V_0 + \alpha x$, the electron momentum is $k(x) = k_0 - ax$, where $k_0 = (\varepsilon - V_0)/\hbar v_F$ and $a = \alpha/\hbar v_F$. From this, we find $\partial_x k(x) = -a$, which becomes a small parameter in expansion. Based on these assumptions, we acquire a second-order differential equation with respect to the first wave-function component $\phi_A(x)$, yielding

$$\partial_x^2\phi_A(x) + \frac{a}{k_0 - ax}\,\partial_x\phi_A(x) + \left[(k_0 - ax)^2 - \frac{ak_y}{k_0 - ax} - k_y^2\right]\phi_A(x) = 0\ . \tag{11}$$

Considering the fact that $|a| \ll 1$, we approximate the above equation as

$$\partial_x^2\phi_A(x) + \left(\frac{a}{k_0} + \frac{a^2 x}{k_0^2}\right)\partial_x\phi_A(x) + \left[k_0^2 - k_y^2 - a\left(\frac{k_y}{k_0} + 2k_0 x\right) + a^2\left(x^2 - \frac{xk_y}{k_0^2}\right)\right]\phi_A(x) = 0\ . \tag{12}$$

Now, let us look for a perturbative solution of Eq. (12) in the form of $\phi_A(x) = \phi_A^{(0)}(x) + a\,\phi_A^{(1)}(x) + a^2\,\phi_A^{(2)}(x) + \cdots$, and include only the terms up to the first non-vanishing linear correction to $\phi_A(x)$. Therefore, we get the 0th and 1st order equations, respectively,

$$a^0: \quad \partial_x^2\phi_A^{(0)}(x) + \left(k_0^2 - k_y^2\right)\phi_A^{(0)}(x) = 0\ , \tag{13}$$

$$a^1: \quad \partial_x^2\phi_A^{(1)}(x) + \left(k_0^2 - k_y^2\right)\phi_A^{(1)}(x) + \frac{1}{k_0}\,\partial_x\phi_A^{(0)}(x) - \left(\frac{k_y}{k_0} + 2k_0 x\right)\phi_A^{(0)}(x) = 0\ . \tag{14}$$

Moreover, making use of the relation in Eq. (4) for two components of the wave function, i.e.,

$$\phi_B(x) = \frac{\partial_x\phi_A(x) - k_y\,\phi_A(x)}{i(k_0 - ax)} \equiv \phi_B^{(0)}(x) + a\,\phi_B^{(1)}(x)\ , \tag{15}$$

we find

$$\phi_B^{(0)}(x) = \frac{-i}{k_0}\left[\partial_x\phi_A^{(0)}(x) - k_y\,\phi_A^{(0)}(x)\right]\ , \tag{16}$$

$$\phi_B^{(1)}(x) = \frac{-i}{k_0^2}\left\{k_0\left[\partial_x\phi_A^{(1)}(x) - k_y\,\phi_A^{(1)}(x)\right] + x\left[\partial_x\phi_A^{(0)}(x) - k_y\phi_A^{(0)}(x)\right]\right\}\ . \tag{17}$$

Consequently, for the 0th order solution, we are dealing with the tilting-free case having $a = 0$ or a square barrier $V_B(x) = V_0$. From Eq. (13) we easily find its solution

$$\phi_A^{(0)}(x) = c_1^{(0)}\mathtt{e}^{ik_x x} + c_2^{(0)}\mathtt{e}^{-ik_x x} \qquad \text{with } k_x = \sqrt{k_0^2 - k_y^2}\ , \tag{18}$$

which is a superposition of the forward and backward plane waves. [2] In this case, from Eq. (16) the corresponding solution for the second component of the wave function is given by

$$\begin{aligned}\phi_B^{(0)}(x) \quad &= c_1^{(0)}\left(\frac{k_x + ik_y}{\gamma\,k_0}\right)\mathtt{e}^{ik_x x} + c_2^{(0)}\left(\frac{-k_x + ik_y}{\gamma\,k_0}\right)\mathtt{e}^{-ik_x x} \\ &\equiv \gamma\left(c_1^{(0)}\,\mathtt{e}^{i\theta_{\mathbf{k}}}\,\mathtt{e}^{ik_x x} - c_2^{(0)}\,\mathtt{e}^{-i\theta_{\mathbf{k}}}\,\mathtt{e}^{-ik_x x}\right)\ ,\end{aligned} \tag{19}$$

where $\gamma = \mathrm{sign}\,(\varepsilon - V_0) = \pm 1$ is the electron-hole index within the barrier region and $\theta_{\mathbf{k}} = \tan^{-1}(k_y/k_x)$ for Dirac electrons inside the barrier region. Assuming $\varepsilon > V_0$, we always have $\gamma > 0$ and no electron-hole switching will occur. Two constants $c_1^{(0)}$ and $c_2^{(0)}$ in Eqs. (18) and (19) can be determined by boundary conditions at both sides of a barrier.

Specifically, the incoming wave function is taken as [2,39,40]

$$\Phi_i(x) = \frac{1}{\sqrt{2}} \begin{bmatrix} \mathsf{e}^{i\phi_{\mathbf{k}}/2} \\ \\ \mathsf{e}^{-i\phi_{\mathbf{k}}/2} \end{bmatrix} \mathsf{e}^{ik_x^{(0)}x} \ , \tag{20}$$

where $V_B(x<0)=0$, $k_x^{(0)} = \sqrt{(\varepsilon/\hbar v_F)^2 - k_y^2}$ and $\phi_{\mathbf{k}} = \tan^{-1}\left(k_y/k_x^{(0)}\right)$ is the incident angle of Dirac electrons. Here, the transversal electron wave number k_y remains as a constant during the whole tunneling process.

Moreover, we notice that $c_1^{(0)}$ and $c_2^{(0)}$ in Eqs. (18) and (19) are not normalized, and they can be determined by the continuity boundary condition at $x=0$, leading to

$$\begin{aligned} c_1^{(0)} &= \frac{\left[\gamma + \mathsf{e}^{i(\phi_{\mathbf{k}}+\theta_{\mathbf{k}})}\right]\ \left(1+\mathsf{e}^{2i\phi_{\mathbf{k}}}\right)}{\mathbb{D}(k_x,\phi_{\mathbf{k}}\,|\,\theta_{\mathbf{k}})} \ , \\ c_2^{(0)} &= \frac{\mathsf{e}^{i(2k_xW_B+\theta_{\mathbf{k}})}\ \left(1+\mathsf{e}^{2i\phi_{\mathbf{k}}}\right)\ \left(\gamma\,\mathsf{e}^{i\theta_{\mathbf{k}}} - \mathsf{e}^{i\phi_{\mathbf{k}}}\right)}{\mathbb{D}(k_x,\phi_{\mathbf{k}}\,|\,\theta_{\mathbf{k}})} \ , \\ \mathbb{D}(k_x,\phi_{\mathbf{k}}\,|\,\theta_{\mathbf{k}}) &= \gamma + \mathsf{e}^{i(\phi_{\mathbf{k}}+\theta_{\mathbf{k}})}\left[2+\gamma\,\mathsf{e}^{i(\phi_{\mathbf{k}}+\theta_{\mathbf{k}})}\right] \\ &+ \ 2\,\mathsf{e}^{i(2k_xW_B+\phi_{\mathbf{k}}+\theta_{\mathbf{k}})}\left[\gamma\cos\left(\theta_{\mathbf{k}}-\phi_{\mathbf{k}}\right)-1\right] \ . \end{aligned} \tag{21}$$

Here, $c_1^{(0)}$ and $c_2^{(0)}$ in Eq. (18) play the role of transmission and reflection amplitudes, respectively, within the barrier region. Using the result in Eq. (21) and the continuity boundary condition at $x=W_B$ as well, we can further calculate the transmission coefficient $t^{(0)}$ as

$$t^{(0)} = \frac{\gamma\,\mathsf{e}^{-ik_xW_B}\ \cos\theta_{\mathbf{k}}\ \cos\phi_{\mathbf{k}}}{\gamma\ \cos(k_xW_B)\ \cos\theta_{\mathbf{k}}\ \cos\phi_{\mathbf{k}} + i\sin(k_xW_B)\ (\gamma\ \sin\theta_{\mathbf{k}}\ \sin\phi_{\mathbf{k}}-1)} \ , \tag{22}$$

which is identical to the corresponding results in Ref. [2] for a square barrier.

In a similar way, we can find the 1st order solution from Eq. (14) for $\phi_A^{(1)}(x)$, yielding

$$\begin{aligned} \phi_A^{(1)}(x) &= c_1^{(1)}\mathsf{e}^{ik_xx} + c_2^{(1)}\mathsf{e}^{-ik_xx} + \mathcal{F}(x\,|\,k_x,\theta_{\mathbf{k}}) \qquad \text{with} \\ \mathcal{F}(x\,|\,k_x,\theta_{\mathbf{k}}) &= \frac{\mathsf{e}^{-ik_xx}}{4k_x^3}\left\{c_2^{(0)}\Big(-k_x\mathsf{e}^{-\theta_{\mathbf{k}}}\left(2k_xx-i\right)+k_0\left[2k_xx\left(1+ik_xx\right)-i\right]\Big)\right. \\ &+ \left. i\,c_1^{(0)}\mathsf{e}^{2ik_xx}\ \Big(-ik_x\mathsf{e}^{+\theta_{\mathbf{k}}}\left(2k_xx+i\right)+k_0\left[2k_xx\left(k_xx+i\right)-1\right]\Big)\right\} \ . \end{aligned} \tag{23}$$

Here, the two new undetermined constants $c_1^{(1)}$ and $c_2^{(1)}$ are completely different from the zero-order constants $c_1^{(0)}$ and $c_2^{(0)}$ in Eq. (21), and they physically represent the first-order corrections to transmission and reflection amplitudes inside the barrier region. By using these computed first wave-function components $\phi_A^{(0)}(x)$ and $\phi_A^{(1)}(x)$ in Eqs. (18) and (23), it is straightforward to find the second wave-function component $\phi_B^{(1)}(x)$ from Eq. (17) although its explicit expression becomes too tedious to write out.

Now, we are able to determine the coefficients $c_1^{(1)}$ and $c_2^{(1)}$ in Eq. (23) and the correction $t^{(1)}$ to the transmission coefficient $t^{(0)}$ in Eq. (22). Corresponding to the wave functions in Eqs. (17) and (23), we can express the transmission and reflection coefficients as $t = t^{(0)} + a\,t^{(1)}$ and $r = r^{(0)} + a\,r^{(1)}$, respectively. Using the two boundary conditions at $x=0$ and $x=W_B$, we arrive at two equations for $r^{(1)}$ and $t^{(1)}$, given by

$$\begin{aligned} r^{(1)}\begin{bmatrix} 1 \\ \\ -\mathsf{e}^{-i\phi_{\mathbf{k}}} \end{bmatrix} &= \begin{bmatrix} \phi_A^{(1)}(x=0\,|\,k_x,\theta_{\mathbf{k}}) \\ \\ \phi_B^{(1)}(x=0\,|\,k_x,\theta_{\mathbf{k}}) \end{bmatrix} \ , \qquad \text{and} \\ t^{(1)}\begin{bmatrix} 1 \\ \\ \mathsf{e}^{i\phi_{\mathbf{k}}} \end{bmatrix}\mathsf{e}^{ik_x^{(0)}W_B} &= \begin{bmatrix} \phi_A^{(1)}(x=W_B\,|\,k_x,\theta_{\mathbf{k}}) \\ \\ \phi_B^{(1)}(x=W_B\,|\,k_x,\theta_{\mathbf{k}}) \end{bmatrix}\mathsf{e}^{ik_xW_B} \ . \end{aligned} \tag{24}$$

Finally, the transmission amplitude $T(\varepsilon,\phi_{\mathbf{k}}\,|\,V_0,\alpha)$ can be simply found from $T(\varepsilon,\phi_{\mathbf{k}}\,|\,V_0,\alpha)=|t^{(0)}+at^{(1)}|^2$, where $t^{(0)}$ and $t^{(1)}$ are presented in Eqs. (22) and (24).

Mathematically, our obtained perturbative solution in subsection II B holds only for a small barrier tilting. However, the expressions in Eqs. (9) and (10) represent the general solutions to Dirac-electron tunneling through a tilted barrier in WKB approximation. We present the numerical results of Eqs. (9) and (10) for a large barrier tilting in panels (a) and (b) of Fig. 2. Here, a large graphene gap Δ_G significantly suppresses $T(\varepsilon,\phi_{\mathbf{k}}\,|\,V_0,\alpha)$ for all values of a, as shown in Fig. 2(a), while the increase of tilting parameter a enhances $T(\varepsilon,\phi_{\mathbf{k}}\,|\,V_0,\alpha)$ for all values of Δ_G, as seen in Fig. 2(b). From Figs. 2(c) and 2(e), we further find that the full transmission for a head-on collision remains unchanged even for a tilted barrier with $a\neq 0$. For small a values, the electron-hole transition does not take place within the barrier region. In this case, a finite a only slightly modifies the resonances of oblique tunneling but not the Klein paradox for the head-on collision.

III. EFFECT OF SCATTERS ON DIRAC-ELECTRON TUNNELING

In this Section, we would concentrate on studying effects of distributed scatters within a tilted barrier region on the ballistic transport of Dirac electrons in gapped graphene. For this purpose, we first lay out the general formalism based on a finite-difference approach (FDA) for any barrier potentials. As an example, we apply the FDA to reveal scatter effects on Dirac-electron tunneling, including different scatter strengths and positions. The main advantage of the FDA is its capability to determine exact electron wave functions for arbitrary potential profiles. [38]

We will consider both cases with a zero or finite energy gap for graphene. Technically, an energy gap ($\sim 200\,$meV) could be introduced by placing a graphene sheet on top of either insulating silicon-based [41] or hexagonal boron-nitride substrate. [42] It could also be realized by patterned hydrogen adsorption [43] or imposing a circularly-polarized off-resonance laser field.[44,45] This gap opening leads to substantial modifications of electronic states, electric transport and collective properties of graphene, e.g., plasmon dispersions. [46–48]

A. Electronic States of Gapped Graphene

For gapped graphene, there exists a finite energy bandgap $E_G=2\Delta_G$ between the valence and conduction bands with energy dispersion $\varepsilon_\gamma(k)=\gamma\sqrt{(\hbar v_F k)^2+\Delta_G^2}$, where $\gamma=\pm 1$ correspond to electron and hole state, respectively. The Hamiltonian matrix associated with this dispersion possesses an additional $\hat{\Sigma}_z$ term on top of the Dirac Hamiltonian for gapless graphene, [39,48] yielding

$$\hat{\mathcal{H}}_g(\boldsymbol{r})=-iv_F\,\hat{\boldsymbol{\Sigma}}_{x,y}\cdot\boldsymbol{\nabla}_{\mathbf{r}}+V_B(x)\,\hat{\Sigma}_0+\Delta_G\,\hat{\Sigma}_z\ , \tag{25}$$

where $\boldsymbol{r}=\{x,y\}$, $\hat{\Sigma}_{x,y,z}$ are two-dimensional Pauli matrices, $\hat{\Sigma}_0$ is a (2×2) unit matrix, and $V_B(x)$ represents an arbitrary spatially-nonuniform barrier potential.

In general, the scattering-state solution for the Hamiltonian in Eq. (25) has a two-component (spinor) type of wave function $\Psi_\gamma(\boldsymbol{r})=\mathtt{exp}(ik_y y)\,\Phi_\gamma(x)=\mathtt{exp}(ik_y y)\,[\phi_A^\gamma(x),\,\phi_B^\gamma(x)]^T$, where $\gamma=\mathrm{sign}[\varepsilon_0(k)-V_B(x)]=\pm 1$ represents the electron-hole index and $\varepsilon_0(k)$ is the given energy of an incident electron.

For the case with a constant barrier potential V_0, however, the Hamiltonian in Eq. (25) can be greatly simplified as

$$\hat{\mathcal{H}}_g^{(0)}(k\,|\,\theta_{\mathbf{k}})=\begin{bmatrix} V_0+\Delta_G & \hbar v_F k_- \\ \hbar v_F k_+ & V_0-\Delta_G \end{bmatrix}\ , \tag{26}$$

where $\boldsymbol{k}=(k_x^{(0)},k_y)$ and $k_\pm=k_x^{(0)}\pm ik_y$. In this case, the scattering-state wave function related to the Hamiltonian in Eq. (26) gains the explicit form [39,49]

$$\Psi_\gamma^{(0)}(\boldsymbol{r})=\frac{1}{\sqrt{2\gamma\,\delta\varepsilon_0(k)}}\begin{bmatrix} \sqrt{|\delta\varepsilon_0(k)+\Delta_G|} \\ \gamma\sqrt{|\delta\varepsilon_0(k)-\Delta_G|}\,\mathtt{e}^{i\theta_{\mathbf{k}}} \end{bmatrix}\mathtt{exp}(ik_x^{(0)}x+ik_y y)\ , \tag{27}$$

where $\theta_{\mathbf{k}} = \tan^{-1}(k_y/k_x^{(0)})$, $\delta\varepsilon_0(k) \equiv \varepsilon_0(k) - V_0 \geq \Delta_G$ for $\gamma = +1$, while $\delta\varepsilon_0(k) \leq -\Delta_G$ for $\gamma = -1$. Here, two components of the wave function in Eq. (27) are not the same but they are still interchangeable for electrons and holes with $\gamma = \pm 1$.

B. Effects of Barrier-Distributed Scatters

For the Hamiltonian in Eq. (25), a pair of scattering-state equations within the barrier region are derived as

$$\begin{aligned}
\frac{d\phi_B(x)}{dx} + k_y\,\phi_B(x) &= \frac{i}{\hbar v_F}\,\left[\varepsilon_0(k) - V_B(x) + V_s\,\delta(x - x_s) - \Delta_G\right]\phi_A(x)\ , \\
\frac{d\phi_A(x)}{dx} - k_y\,\phi_A(x) &= \frac{i}{\hbar v_F}\,\left[\varepsilon_0(k) - V_B(x) + V_s\,\delta(x - x_s) + \Delta_G\right]\phi_B(x)\ .
\end{aligned} \tag{28}$$

Here, we consider a barrier under a tilting field $\mathcal{E}_0$, which gives rise to $V_B(x) = V_0 - e\mathcal{E}_0\,x$ in the barrier region, where both V_0 and $\mathcal{E}_0$ can be either positive or negative. Additionally, k_y of electrons remains conserved during a tunneling process along the x direction. Moreover, a single scatter at $0 < x = x_s < W_B$ is introduced within the barrier region with its strength $-V_s$, which can be positive (attractive) or negative (repulsive).

Mathematically, we can divide the electron wave function corresponding to three separated regions. To the left of the barrier $x < 0$, we acquire the wave function

$$\Phi_<(x) = s(\varepsilon_0)\begin{bmatrix} 1 \\ \mathsf{e}^{i\phi_{\mathbf{k}}} \end{bmatrix}\mathtt{exp}(ik_x^{(0)}x) + r(\varepsilon_0)\begin{bmatrix} 1 \\ -\mathsf{e}^{i\phi_{\mathbf{k}}} \end{bmatrix}\mathtt{exp}(-ik_x^{(0)}x)\ , \tag{29}$$

where $\phi_{\mathbf{k}} = \tan^{-1}(k_y/k_x^{(0)})$, $s(\varepsilon_0)$ and $r(\varepsilon_0)$ represent incoming and reflected wave-function amplitudes. To the right of the barrier $x > W_B$, on the other hand, the wave function takes the form

$$\Phi_>(x) = t(\varepsilon_0')\begin{bmatrix} 1 \\ \mathsf{e}^{i\phi_{\mathbf{k}'}} \end{bmatrix}\mathtt{exp}(ik_x'x)\ , \tag{30}$$

where $\phi_{\mathbf{k}'} = \tan^{-1}(k_y/k_x')$ and $t(\varepsilon_0')$ is the transmitted wave-function amplitude.

Results in Eqs. (29) and (30) can be applied to construct boundary conditions on both sides of a barrier. For the wave function within the barrier region, however, the FDA must be employed to seek for a numerical solution of Eq. (28). Following the procedure adopted in Ref. [38] for a two-dimensional electron gas, we discrete the whole barrier region $0 \leq x \leq W_B$ into N_B (odd integer) equally spaced slabs, and each slab has the same width $\Delta_0 = W_B/N_B$. Consequently, two coupled differential equations in Eq. (28) can be solved simultaneously through a backward-iteration procedure in combination with two continuity boundary conditions at $x = W_B$ and $x = 0$. Especially, as $\Delta_G = 0$ we find the following backward iterative relation for $1 \leq j \leq N_B + 1$ and $x_j = (j-1)\Delta_0$, i.e.,

$$\begin{Bmatrix} \phi_A(x_{j-1}) \\ \phi_B(x_{j-1}) \end{Bmatrix} = \begin{Bmatrix} \phi_A(x_j) \\ \phi_B(x_j) \end{Bmatrix} - k_y\Delta_0\begin{Bmatrix} \phi_A(x_j) \\ -\phi_B(x_j) \end{Bmatrix} + \frac{i\Delta_0}{\hbar v_F}\left[\varepsilon_0(k) - V_0 + e\mathcal{E}_0x_j + V_s\,\delta(x_j - x_s)\right]\begin{Bmatrix} \phi_B(x_j) \\ \phi_A(x_j) \end{Bmatrix}\ , \tag{31}$$

where $V_s = V_d\,\Delta_0$ and V_d represents the point-scatter potential.

By using Eq. (30), the first continuity boundary condition at $x_{N_B+1} = W_B = N_B\Delta_0$ leads to

$$\begin{Bmatrix} \phi_A(x_{N_B+1}) \\ \phi_B(x_{N_B+1}) \end{Bmatrix} = t(\varepsilon_0'(k'))\begin{Bmatrix} 1 \\ \mathsf{e}^{i\phi_{\mathbf{k}'}} \end{Bmatrix}\mathtt{exp}(ik_x'N_B\Delta_0)\,\mathtt{exp}\left[k_y\Delta_0\sum_{j=2}^{N_B+1}\Theta(-\kappa(x_j))/\sqrt{|\kappa(x_j)|}\right]_{x_j\neq x_D}\ , \tag{32}$$

where $\kappa(x_j) = \left[(1/\hbar v_F)\,(\varepsilon_0(k) - V_0 + e\mathcal{E}_0x_j)\right]^2 - k_y^2$, $\varepsilon_0'(k') = \hbar v_F\sqrt{k_x'^2 + k_y^2} = \varepsilon_0(k) + e\mathcal{E}_0W_B$, and $\Theta(x)$ is a unit-step function. Physically, the last exponential factor in Eq. (32) does not affect the transmission coefficient if $\kappa(x_j) > 0$,

corresponding to a semi-classical regime. However, this factor can significantly reduce the transmission coefficient, but not the reflection coefficient, if $\kappa(x_j) < 0$, connecting to a quantum-tunneling regime. The backward iteration in Eq. (31) can be performed all the way down to $x_1 = 0$.

In a similar way, using Eq. (29) and another continuity boundary condition at $x_1 = 0$, we find

$$\left\{ \begin{array}{c} |s(\varepsilon_0)|^2 \\ \\ |r(\varepsilon_0)|^2 \end{array} \right\} = \frac{1}{4} \left\{ \begin{array}{l} |a|^2 + |b|^2 + 2\mathtt{Re}(ab^* \mathtt{e}^{i\phi_{\mathbf{k}}}) \\ \\ |a|^2 + |b|^2 - 2\mathtt{Re}(ab^* \mathtt{e}^{i\phi_{\mathbf{k}}}) \end{array} \right\} , \tag{33}$$

where we have defined the notations

$$\left\{ \begin{array}{c} a \\ \\ b \end{array} \right\} \equiv \left\{ \begin{array}{c} \phi_A(x_1) \\ \\ \phi_B(x_1) \end{array} \right\} = s(\varepsilon_0) \left\{ \begin{array}{c} 1 \\ \\ \mathtt{e}^{i\phi_{\mathbf{k}}} \end{array} \right\} + r(\varepsilon_0) \left\{ \begin{array}{c} 1 \\ \\ -\mathtt{e}^{i\phi_{\mathbf{k}}} \end{array} \right\} . \tag{34}$$

The transmission coefficient $T(k, \phi_{\mathbf{k}} \,|\, \mathcal{E}_0, V_d, x_s)$, which is defined as the ratio of the transmitted to the incident probability current densities, [1,2] is given by

$$T(k, \phi_{\mathbf{k}} \,|\, \mathcal{E}_0, V_d, x_s) = \frac{|t(\varepsilon_0')|^2}{|s(\varepsilon_0)|^2} , \tag{35}$$

since electrons on both sides of the barrier have the same group velocity v_F. Numerically, it is easy to set $t(\varepsilon_0') \equiv 1$, then to find $s(\varepsilon_0)$ through Eq. (34) after having performed all the backward iterations, and finally obtain the ratio in Eq. (35).

Using the calculated transmission coefficient in Eq. (35), we are able to compute the coherent-tunneling electric current J_0 per length, yielding

$$J_0 = \frac{4e}{\mathcal{A}} \sum_{\mathbf{k}} T(k, \phi_{\mathbf{k}} \,|\, \mathcal{E}_0, V_d, x_s)\, v_F \cos\phi_{\mathbf{k}} \left[f_0(\varepsilon_0(k)) - f_0(\varepsilon_0(k) + e\mathcal{E}_{dc} W_B) \right] , \tag{36}$$

where $\mathcal{E}_{dc}$ is a weak applied bias field between two electrodes, $\mathcal{A}$ is the graphene sheet area, $f_0(x) = \{1 + \exp[(x - u_0)/k_B T]\}^{-1}$ is the Fermi function for thermal-equilibrium electrons at temperature T, and $u_0(T)$ is the chemical potential of electrons. For a weak electric field, we have $e\mathcal{E}_{dc} W_B \ll \varepsilon_0(k)$, which leads to

$$J_0 \approx \frac{4e^2 v_F U_0}{\mathcal{A}} \sum_{\mathbf{k}} T(k, \phi_{\mathbf{k}} \,|\, \mathcal{E}_0, V_d, x_s)\, \cos\phi_{\mathbf{k}} \left[-\frac{\partial f_0(\varepsilon_0(k))}{\partial \varepsilon_0} \right] , \tag{37}$$

were $U_0 = \mathcal{E}_{dc} W_B$ represents the voltage drop across the barrier and $U_0/(J_0 \mathcal{A})$ gives rise to tunneling resistance R. If T is low, i.e., $k_B T \ll E_F$ with $E_F = \hbar v_F k_F$ as the zero-temperature u_0 or Fermi energy, we find

$$\begin{aligned} J_0 \;&\approx\; \frac{4e^2 v_F U_0}{\mathcal{A}} \sum_{\mathbf{k}} T(k, \phi_{\mathbf{k}} \,|\, \mathcal{E}_0, V_d, x_s)\, \cos\phi_{\mathbf{k}}\, \delta(\hbar v_F k - E_F) \\ &=\; \frac{U_0}{\pi} \left(\frac{2e^2}{h} \right) \int_0^{\infty} dk\, k\, \delta(k - k_F) \int_{-\pi/2}^{\pi/2} d\phi_{\mathbf{k}}\, T(k, \phi_{\mathbf{k}} \,|\, \mathcal{E}_0, V_d, x_s)\, \cos\phi_{\mathbf{k}} \\ &=\; \mathcal{E}_{dc}\, k_F W_B \left(\frac{2e^2}{h} \right) \left\{ \frac{1}{\pi} \int_{-\pi/2}^{\pi/2} d\phi_{\mathbf{k}}\, T(k_F, \phi_{\mathbf{k}} \,|\, \mathcal{E}_0, V_d, x_s)\, \cos\phi_{\mathbf{k}} \right\} , \end{aligned} \tag{38}$$

where $k_F = \sqrt{\pi n_0}$ is the Fermi wave vector and n_0 is the areal electron doping density. Finally, we obtain the two-terminal sheet tunneling conductivity $\sigma(k_F, \mathcal{E}_0, V_d, x_s)$ (in units of $2e^2/h$), given by [50]

$$\sigma(k_F, \mathcal{E}_0, V_d, x_s) = \frac{J_0}{\mathcal{E}_{dc}} = \frac{k_F W_B}{\pi} \int_{-\pi/2}^{\pi/2} d\phi_{\mathbf{k}}\, T(k_F, \phi_{\mathbf{k}} \,|\, \mathcal{E}_0, V_d, x_s)\, \cos\phi_{\mathbf{k}} \ . \tag{39}$$

Specifically, for normal incidence of electrons with $\phi_{\mathbf{k}} \equiv 0$, we simply get $\sigma_0(k_F, \mathcal{E}_0) = (k_F W_B)\, T(k_F \,|\, \mathcal{E}_0, V_d, x_s)$.

By going beyond a single scatter for the coherent tunneling, to simulate effects of barrier-distributed scatters on the incoherent tunneling of Dirac electrons, we introduce a normal distribution function and replace the transmission coefficient $T(k_F, \phi_{\mathbf{k}} \,|\, \mathcal{E}_0, V_d, x_s)$ in Eqs. (35) and (39) by its average $\overline{T}(k, \phi_{\mathbf{k}} \,|\, \mathcal{E}_0, V_d)$, yielding

$$\overline{T}(k, \phi_{\mathbf{k}} \,|\, \mathcal{E}_0, V_d) = \frac{1}{N_D} \int_0^{W_B} dx_s\, T(k_F, \phi_{\mathbf{k}} \,|\, \mathcal{E}_0, V_d, x_s)\, \rho(x_s \,|\, \xi_s) \approx \frac{\Delta_0}{N_s} \sum_{s=2}^{N_B} T(k_F, \phi_{\mathbf{k}} \,|\, \mathcal{E}_0, V_d, x_s^*)\, \rho(x_s^* \,|\, \xi_s) \ , \tag{40}$$

where $x_s^* = (s-1)\Delta_0$, the introduced scatter distribution function is assumed to be

$$\rho(x_s^* \,|\, \xi_s) = \frac{1}{\sqrt{2\pi\xi_s^2}}\, \exp\left[-\frac{(x_s^* - W_B/2)^2}{2\xi_s^2}\right] \tag{41}$$

with the chosen standard deviation $\xi_s = \Delta_0$ and $W_B/2 = [(N_B+1)/2]\Delta_0$. In addition, the normalization factor in Eq. (40) is given by

$$N_s = \int_0^{W_B} dx_s\, \rho(x_s \,|\, \xi_s) \approx \Delta_0 \sum_{s=2}^{N_B} \rho(x_s^* \,|\, \xi_s) \ . \tag{42}$$

For convenience, in numerical calculations we further approximate the delta-function in Eq. (31) by

$$\delta(x_j - x_s) \equiv \delta(x_j - x_s^*) \approx \frac{\Gamma_s/\pi}{(x_j - x_s^*)^2 + \Gamma_s^2} \tag{43}$$

with another chosen broadening parameter $\Gamma_s = \Delta_0$.

C. Numerical Results and Their Discussions

In Subsection III C, we will present numerical results for demonstrating effects of barrier tilting, single barrier-embedded scatter and continuously-distributed scatters within a barrier, respectively. We also present comparisons and detailed discussion of these results to reveal new physics and highlight the interplay between effects of distributed scatters in a barrier and barrier tilting on tunneling transport of Dirac electrons in graphene.

1. Effect of barrier tilting

For a validation of our FDA, we first compare our numerical results in the absence of scatters ($V_d = 0$) with those from an analytical solution [2] for a square barrier $V_B(x) = V_0$. Figure 3 displays a comparison for calculated transmission coefficients $T(\varepsilon, \phi_{\mathbf{k}} \,|\, \mathcal{E}_0 = 0)$ as a function of incident angle $\phi_{\mathbf{k}}$ using either an analytical solution [2] (black solid curves) or our FDA (red dashed curves). The results in this figure clearly indicate that our FDA is valid and can be applied to arbitrary potential profiles $V_B(x)$ including a tilted barrier or barrier-distributed scatters.

As a starting point, using the FDA we will first explore the effects of barrier tilting on the ballistic transport of Dirac electrons by neglecting barrier-distributed scatters. For this situation, the numerical results of $T(\varepsilon, \phi_{\mathbf{k}} \,|\, \mathcal{E}_0)$ are presented in Fig. 4 as a function of incident angle $\phi_{\mathbf{k}}$ for various values of tilting field $\mathcal{E}_0$. Our results indicate that the Klein paradox, i.e., $T(\varepsilon, \phi_{\mathbf{k}} \,|\, \mathcal{E}_0) = 1$ at $\phi_{\mathbf{k}} = 0$, persists for all considered tilting field $\mathcal{E}_0$ values, either positive

or negative. From this figure we see very-large-angle resonant tunneling only occurs for $|\mathcal{E}_0| \approx 0$. As $|\mathcal{E}_0|$ becomes large, however, resonant tunneling are squeezed into a very narrow angle region around $\phi_{\mathbf{k}} = 0$, promoting tunneling collimation as predicted by WKB result in Eq. (9). Such variations observed in $T(\varepsilon, \phi_{\mathbf{k}} \,|\, \mathcal{E}_0)$ can be attributed to the tilting modification of a barrier potential profile $V_B(x)$ compared with a simple square barrier $V_B(x) = V_0$.

Figure 5 displays density plots of $T(\varepsilon, \phi_{\mathbf{k}} \,|\, \mathcal{E}_0)$ as functions of both incident energy ε and incident angle $\phi_{\mathbf{k}}$ with six different values for tilting field $\mathcal{E}_0$. Here, we take the case with $\mathcal{E}_0 = 0$ as a starting point for our comparisons and discussions, where the Klein paradox and collimation effect exist accompanied by many sharp resonances (i.e., branching and needling features). As $\mathcal{E}_0$ increases from zero to 25 kV/m in the upper row of panels for reduced barriers, these resonant branching and needling features are greatly obscured although the Klein paradox persists. On the other hand, as $\mathcal{E}_0$ decreases from zero to -35 kV/m in the low row of panels for enhanced barriers, both branching and needling regions expand significantly to higher incident energies of electrons.

The calculated tunneling coefficient $T(\varepsilon, \phi_{\mathbf{k}} \,|\, \mathcal{E}_0)$ can be put into Eq. (39) to find tunneling conductivity or resistivity (its inverse) for coherent tunneling of Dirac electrons through a tilted barrier in graphene in the absence of scatters. Here, the resistivity strongly depends on the tilting field $\mathcal{E}_0$ due to $\mathcal{E}_0$ dependence in $T(\varepsilon, \phi_{\mathbf{k}} \,|\, \mathcal{E}_0)$. For ballistic Dirac electrons in the absence of a barrier, their conductivity should be integer multiple of $2e^2/h$, as indicated by Eq. (39). In the presence of scattering by impurities or phonons, the occurring resistive force will lead to a tilting-dependent conductivity which is accompanied by joule heating of electrons [51,52]. Here, however, a tilting-dependent conductivity is induced by a tunneling barrier which only reflects incoming electrons elastically and coherently, leading to a destructive interference. Such a behavior can be attributed to a strongly-modulated barrier tilting ($\mathcal{E}_0$ dependence) in tunneling coefficient $T(\varepsilon, \phi_{\mathbf{k}} \,|\, \mathcal{E}_0)$, as shown in Eq. (39).

In Fig. 6, we present the calculated resistance ratios R/R_0 as functions of incident electron energy ε for different decreasing (left panel) and increasing (right panel) tilted barriers. We find from this figure that the resistance peak height decreases with increasing positive $\mathcal{E}_0$ and the peak position shifts down to lower incident energy ε at the same time. For increasing negative $\mathcal{E}_0$, on the other hand, the peak position shifts upward with ε but the peak height remains nearly unchanged. Furthermore, the resistance peak is broadened with increasing $|\mathcal{E}_0|$, and the broadening effect becomes much stronger for negative $\mathcal{E}_0$ values. Such a resonant feature in ε dependence provides a unique opportunity for controlling tunneling current of Dirac electrons by choosing different Fermi energies E_F or doping densities n_0 in graphene.

As shown in Fig. 7, the transmission coefficient $T(\varepsilon, \phi_{\mathbf{k}} \,|\, \mathcal{E}_0)$ at $\mathcal{E}_0 = 5$ kV/m (reduced barrier) is suppressed only for large incident angles $|\phi_{\mathbf{k}}|$ with increasing barrier width W_B due to enlarged switching from a semi-classical regime to a quantum-tunneling regime inside barrier region, as well as due to increased interference effect in reflections from both barrier edges. Meanwhile, the major peak of $T(\varepsilon, \phi_{\mathbf{k}} \,|\, \mathcal{E}_0)$ for $|\phi_{\mathbf{k}}|$ around zero becomes sharper with more and more suppressed side peaks, leading to enhanced collimation of Dirac-electron tunneling with increasing barrier width.

2. Effect of single barrier-embedded scatter

As a next step, using the same FDA we will further explore the effect from a single barrier-embedded scatter on the coherent tunneling of Dirac electrons by neglecting first the barrier tilting or simply setting $\mathcal{E}_0 = 0$. As displayed in Fig. 8, we learn from the left panel that the presence of a single scatter in the barrier region can dramatically enhance the collimation of Dirac-electron tunneling with $x_s = W_B/2$, and such effect is weakened as we move the scatter away from the barrier center. On the other hand, if we vary the scatter strength V_d from positive (attractive) to negative (repulsive), we find from the right panel that an attractive scatter tends to collimate better the tunneling of Dirac electrons in comparison with a repulsive scatter. All the features demonstrated in Fig. 8 imply a full control over enhancement in collimating tunneling of Dirac electrons by using a single barrier-embedded scatter for a fixed incident energy.

The left panel of Fig. 9 presents a density plot for $T(\varepsilon, \phi_{\mathbf{k}} \,|\, \mathcal{E}_0, V_d, x_s)$ as functions of both ε and $\phi_{\mathbf{k}}$ for a single scatter embedded in a square barrier at $x_s = W_B/2$, from which we observe a new strong and sharp resonance around $\varepsilon \approx V_0$ by comparing with the upper-left panel of Fig. 5 for $\mathcal{E}_0 = 0$ and no scatter. In the right panel of Fig. 9, we further present a comparison of the tunneling-resistance ratios R/R_0 as a function of incident energy ε for three different positions of a barrier-embedded attractive scatter with $V_d = 50$ meV at $x_s = W_B/2$. In connection with a resistance peak appearing around $\varepsilon/V_0 \approx 1$ for no scatter, the inclusion of an attractive scatter at $x_s = W_B/2$ turns this peak into a very deep cusp surrounded by two asymmetric shoulders. Such an observation can be attributed to the effect from a scatter-induced constructive interference around the Dirac point on the coherent tunneling process of Dirac electrons in the system, as demonstrated by the left panel of this figure. As the scatter is moved away to $x_s = 3W_B/4$, the cusp depth is greatly reduced while symmetrizing two shoulders at the same time. Surprisingly, this deep cusp

changes back to a peak for $x_s = W_B/4$ due to switching to an opposite destructive interference around the Dirac point. The occurrence of such a deep cusp in tunneling resistance in Fig. 9 reveals the effect from coherent superposition of multiple reflections from a single mid-barrier-embedded attractive scatter on tunneling of Dirac electrons as the incident energy approaches the top of a square barrier or the Dirac point within a barrier.

In Fig. 10, we further present a comparison of the tunneling-resistance ratios R/R_0 as a function of ε for five different strengths of a single scatter at $x_s = W_B/2$ in order to show the influence of scatter identity on the coherently superposed multiple reflections from a single scatter at the middle of a barrier. From this figure, we first notice that the cusp remains independent of values of V_d, i.e., either an attractive or a repulsive scatter. Moreover, two shoulders around the cusp become weak with increasing $|V_d|$ values. Interestingly, only the attractive scatter with $V_d = 100\,\text{meV}$ can symmetrize these two shoulders, but not the repulsive scatter with $V_d = -100\,\text{meV}$, in strong contrast to incoherent scattering by randomly-distributed scatters [51,52]. Meanwhile, the depth of a cusp also remains largely unchanged with V_d since it results from a constructive interference around the Dirac point within a barrier due to multiple coherent scatterings from a single scatter at $x_s = W_B/2$, and thus depends only on phase accumulation or scatter position. In the presence of a single mid-barrier scatter, the unique tunneling selection by an incident energy close to the square-barrier top for switching a resistance peak for no scatter to a cusp can be utilized for designing an energy filter for incident Dirac electrons.

3. Effect of continuously-distributed scatters within a barrier

From Figs. 8−10, we have understood that both tunneling transmission coefficient and tunneling resistance can be varied by selecting different positions or strengths for a single scatter embedded in a square barrier. To be more realistic, as a final step, still using the FDA, we would investigate the interplay between continuously-distributed scatters in a barrier and barrier tilting in electric transport of Dirac electrons within a graphene layer. For this purpose, however, a summation over all positions of continuously-distributed scatters within a barrier should be performed for averaging transmission coefficients corresponding to different scatter positions. To facilitate such a summation, we introduce a Gaussian-type distribution function for all of scatters within a barrier, as presented in Eq. (41). Consequently, the obtained average $\overline{T}(k, \phi_{\mathbf{k}} \,|\, \mathcal{E}_0, V_d)$ can be fed into Eq. (39) for calculating incoherent tunneling resistance in the presence of continuously-distributed scatters within a tilted barrier.

We find from the left panel of Fig. 11 for $\varepsilon = 80\,\text{meV}$ that the dramatic changes in $\overline{T}(\varepsilon, \phi_{\mathbf{k}} \,|\, \mathcal{E}_0, V_d)$ only occur within the angle region roughly bounded by $|\phi_{\mathbf{k}}| = \pi/6$, which are accompanied by enhanced collimation of incoherent tunneling through a square barrier containing scatters with strong strengths $V_d = \pm 100\,\text{meV}$. Moreover, this enhancement of collimated tunneling appears relatively larger for attractive scatters (blue curve) compared to that of repulsive scatters (green curve). In the right panel of Fig. 11, on the other hand, we exhibit the $\phi_{\mathbf{k}}$ dependence in $\overline{T}(\varepsilon, \phi_{\mathbf{k}} \,|\, \mathcal{E}_0, V_d)$ for different values of $\mathcal{E}_0$ in order to uncover the physics for competition between continuously-distributed scatters within a barrier and tilting field $\mathcal{E}_0$. By comparing with the blue curve for $\mathcal{E}_0 = 0$ in the left panel of this figure, as $\mathcal{E}_0$ increases from zero in the right panel, the continuously-distributed scatters within a barrier gradually exclude more and more high-$\phi_{\mathbf{k}}$ contributions to $\overline{T}(\varepsilon, \phi_{\mathbf{k}} \,|\, \mathcal{E}_0, V_d)$ until all side peaks are completely quenched (purple curve) for a fully collimated tunneling. This incoherent-tunneling result is quite different from that for coherent tunneling in the left panel of Fig. 8 for a single scatter embedded in a square barrier or no scatters at all. The features in Fig. 11 demonstrate in details interplaying between effects of distributed scatters in a barrier and barrier tilting on incoherent tunneling of Dirac electrons in graphene.

To acquire a full understanding about the competition between effects of distributed scatters and barrier tilting on ballistic transport of Dirac electrons, we present in Fig. 12 the dependence of tunneling resistance R/R_0 on the incident energy ε of electrons for different scatter strengths V_d (left) or barrier tilting fields $\mathcal{E}_0$ (right). From the left panel of Fig. 12, we first observe that the cusp as well as two shoulders, which result from a single mid-barrier scatter as seen in Fig. 10 for a square barrier, disappear and are replaced by a single robust peak for $|V_d| \leq 50\,\text{meV}$. As $V_d = 100\,\text{meV}$ for the attractive-scatter distribution, this tunneling-resistance peak shifts to lower energy in comparison with the weakened upward-shifting peak for the repulsive-scatter distribution at $V_d = -100\,\text{meV}$. Here, the effect from a mid-barrier-scatter induced constructive interference around the Dirac point, as seen in Fig. 10 for a square barrier, has been fully suppressed due to incoherent-tunneling nature for distributed scatters in a barrier. In the right panel of Fig. 12, we further examine the role of barrier tilting played in incoherent tunneling transport of Dirac electrons in the presence of continuously-distributed attractive scatters within a barrier. From this panel, we find the single peak in the left panel for the square barrier shifts down in energy due to reduction of the effective barrier height with increasing $\mathcal{E}_0$ from zero. Moreover, multiple side peaks appear only on the low-energy shoulder, while their strengths decrease, as $\mathcal{E}_0$ goes up from zero.

IV. SUMMARY AND REMARKS

In summary, to gain insight about the tunneling mechanism of Dirac electrons in graphene, we have first employed a WKB perturbation theory for studying electron transmission through a slanted barrier with a weak tilting field compared to the inverse barrier width and characteristic electron momenta. Based on the WKB approximation, we have derived a set of equations, corresponding to different orders of expansion parameter, and obtained analytical solutions of these equations at the same time. From analysis of these explicit solutions, we have demonstrated how the tunneling resonances of a square barrier are affected by applying a tilting field. Physically, we have extended a previously developed WKB theory for electron transmission in the opposite limit for a large tilting field, in which electron-to-hole switching occurs within the barrier region. Moreover, a finite energy gap in graphene is included and we have shown that both head-on and skew transmissions will be suppressed exponentially in the presence of an energy gap and a large transverse momentum.

Going beyond a slanted barrier, we have further developed a full numerical approach based on the finite-difference approach for accurately calculating tunneling transport of Dirac electrons through an arbitrary barrier potential. Here, the combination of a barrier tilting field and a local scatter potential can be viewed as an effective barrier profile realized by a series of gate combinations. By using this finite-difference approach, Dirac-electronic tunneling and transport properties have been investigated for graphene with an in-plane tilted potential barrier embedded with distributed scatters. In the presence of either a single or a continuous distribution of scatters within a tilted barrier, both transmission coefficient and tunneling resistance of Dirac electrons are calculated numerically. Based on these numerical results, we have presented a full analysis as well as a detailed comparison for the interplay between effects of distributed scatters in a barrier and barrier tilting on tunneling transport of Dirac electrons. We have found from the comparison that the barrier-tilting field, also the scatter position, can play a key role in controlling the peak in tunneling resistance and the peak switching to a cusp by a single mid-barrier scatter as the incident electron energy approaches the Dirac point of a barrier. Importantly, from our calculations we predict that a continuous distribution of scatters in a barrier can increase collimating incoherent tunneling under a high barrier-tilting field, and at the same time, will greatly suppress large-angle skew tunneling. Meanwhile, the continuously-distributed scatters also suppress the constructive interference around the Dirac point and turn a cusp into a peak in tunneling resistance as a function of incident energy of electrons.

From the application perspective, our current study implies a tunable filtering of Dirac electrons by a barrier-tilting field for nearly normal incidence, which could be utilized for designing electronic lenses. The uniqueness of this feature is that we can specify a range for incident electron energies used for focusing. Moreover, the tunneling resistance could be reduced and a conductance minimum can be shifted in energy just by controlling titling-field polarity and strength, barrier height and thickness. Therefore, our model system can be employed to tune the refractive index of such an energy barrier in ballistic-electron optics. Furthermore, as the electron incident energy approaches the top of a square barrier, the switching from a peak in tunneling resistance to a cusp appears when a single scatter potential is introduced at the center of a barrier, which is attributed to an induced constructive interference around the Dirac point within a barrier for the coherent tunneling of Dirac electrons and can be used as either an energy blocker or an energy filter simply by adjusting a barrier-potential profile. All these new revealed properties are expected extremely valuable for the development of novel electronic and optical graphene-based devices.

Acknowledgments

D.H. would thank the support from the Air Force Office of Scientific Research (AFOSR). D.H is also supported by the DoD Lab-University Collaborative Initiative (LUCI) program. G.G. would like to acknowledge the support from the Air Force Research Laboratory (AFRL) through Grant #12530960.

Appendix A: Exact Wave Function

In this Appendix, we seek for an exact solution for the electron/hole wave function in the finite-slope region of a barrier, as seen in Fig. 1, with potential $V_B(x) = V_0 + \alpha x$. If two boundaries of the barrier region stay far away from the electron-to-hole crossing point $x = x_0$, i.e., $k(x_0) \approx 0$, the wave function could be written as [14]

$$\Psi^{(B)}(x \,|\, k_y) = \left\{ c_1 \begin{bmatrix} \mathcal{F}(\eta,\zeta) \\ \mathcal{G}(\eta,\zeta) \end{bmatrix} + c_2 \begin{bmatrix} \mathcal{F}^\star(\eta,\zeta) \\ \mathcal{G}^\star(\eta,\zeta) \end{bmatrix} \right\} \mathsf{e}^{ik_y y} \,, \tag{A1}$$

where $\eta(x) = (x - x_0)\sqrt{a}$, $\zeta(k_y) = k_y/\sqrt{a}$, the symbol * means taking complex conjugation, and the two arbitrary constants c_1 and c_2 will be fixed by the boundary conditions on each side of the barrier region. Moreover, two functions $\mathcal{F}(\eta,\zeta)$ and $\mathcal{G}(\eta,\zeta)$ in Eq. (A1) can be expressed explicitly by a Kummer confluent hypergeometric function $\mathcal{M}(a,b\,|\,z)$ as [14]

$$\begin{aligned}\mathcal{F}(\eta,\zeta) &= \mathtt{exp}\left(-\frac{i}{2}\,\eta^2\right)\,\mathcal{M}\left(-\frac{i}{4}\,\zeta^2,\,\frac{1}{2}\,\Big|\,i\eta^2\right)\,, \\ \mathcal{G}(\eta,\zeta) &= -\zeta\eta\,\mathtt{exp}\left(-\frac{i}{2}\,\eta^2\right)\,\mathcal{M}\left(1-\frac{i}{4}\,\zeta^2,\,\frac{3}{2}\,\Big|\,i\eta^2\right)\,.\end{aligned} \tag{A2}$$

The wave functions outside of the barrier region are easily obtained for the incoming and reflected waves, yielding

$$\Psi^{(L)}(x\,|\,\boldsymbol{k}) = \frac{1}{2}\begin{bmatrix}\mathtt{e}^{i\phi_{\mathbf{k}}}\\ \pm 1\end{bmatrix}\mathtt{e}^{ik_x^{(0)}x}\,\mathtt{e}^{ik_y y} + \frac{r_{\mathbf{k}}}{2}\begin{bmatrix}-\mathtt{e}^{-i\phi_{\mathbf{k}}}\\ \pm 1\end{bmatrix}\mathtt{e}^{-ik_x^{(0)}x}\,\mathtt{e}^{ik_y y}\,, \tag{A3}$$

where $\phi_{\mathbf{k}} = \tan^{-1}(k_y/k_x^{(0)})$. Similarly, for the transmitted wave we have

$$\Psi^{(R)}(x\,|\,\boldsymbol{k}') = \frac{t_{\mathbf{k}'}}{2}\begin{bmatrix}\mathtt{e}^{i\theta_{\mathbf{k}'}}\\ \pm 1\end{bmatrix}\mathtt{e}^{ik_x x}\,\mathtt{e}^{ik_y y}\,, \tag{A4}$$

where $\theta_{\mathbf{k}'} = \tan^{-1}(k_y/k_x)$. The transmission coefficient $t_{\mathbf{k}'}$ and the reflection coefficient $r_{\mathbf{k}}$ can be obtained by matching the wave functions at two boundaries at $x = 0$ and $x = W_B$, i.e., $\Psi^{(B)}(x = 0\,|\,k_y) = \Psi^{(L)}(x = 0\,|\,\boldsymbol{k})$ and $\Psi^{(B)}(x = W_B\,|\,k_y) = \Psi^{(R)}(x = W_B\,|\,\boldsymbol{k}')$. Therefore, we acquire four equations for these two-component wave functions, which can be used to determine four unknowns c_1, c_2, $r_{\mathbf{k}}$ and $t_{\mathbf{k}'}$, and the calculated $t_{\mathbf{k}'}$ can be further employed for evaluating the transmission $T_{\mathbf{k}'} = |t_{\mathbf{k}'}|^2$.

Here, we would like to emphasize that although the obtained solution in Eq. (A1) is exact, it holds true only for a very thick barrier satisfying $0 \ll x_0 \ll W_B$. Additionally, using this approach we can not address the limiting case with a small slope $a \to 0$.

For the boundaries of a very thick barrier with a substantial slope α, we find vary large absolute value of $\eta(x) = (x - x_0)\sqrt{a}$, and the wave function reduces to

$$\begin{aligned}\lim_{\eta\to\infty}\,\Psi^{(B)}(x,\,|\,k_y) &= \begin{bmatrix}0\\ 1\end{bmatrix}\,\mathtt{exp}\left[-\frac{i}{2}\eta^2(x)\right]\,\mathtt{e}^{ik_y y}\,, \\ \lim_{\eta\to-\infty}\,\Psi^{(B)}(x,\,|\,k_y) &= \mathtt{e}^{ik_y y}\,\left\{\mathtt{exp}\left[-\frac{\pi}{2a}\,k_y^2\right]\,\begin{bmatrix}0\\ 1\end{bmatrix}\,\mathtt{exp}\left[-\frac{i}{2}\,\eta^2(x)\right] + const\,\begin{bmatrix}0\\ 1\end{bmatrix}\,\mathtt{exp}\left[\frac{i}{2}\,\eta^2(x)\right]\right\}\,,\end{aligned} \tag{A5}$$

which leads to the transmission $T_{\mathbf{k}'} = \mathtt{exp}\left(-\pi k_y^2/a\right)$. This result is the same as that obtained from a semi-classical theory.

[1] M. Katsnelson and K. Novoselov, Solid State Communications **143**, 3 (2007).
[2] A. C. Neto, F. Guinea, N. M. Peres, K. S. Novoselov, and A. K. Geim, Reviews of modern physics **81**, 109 (2009).
[3] S. D. Sarma, S. Adam, E. Hwang, and E. Rossi, Reviews of modern physics **83**, 407 (2011).
[4] K. S. Novoselov, A. K. Geim, S. Morozov, D. Jiang, M. I. Katsnelson, I. Grigorieva, S. Dubonos, Firsov, and AA, nature **438**, 197 (2005).
[5] K. Wang, M. M. Elahi, L. Wang, K. M. Habib, T. Taniguchi, K. Watanabe, J. Hone, A. W. Ghosh, G.-H. Lee, and P. Kim, Proceedings of the National Academy of Sciences **116**, 6575 (2019).
[6] T. Low and J. Appenzeller, Physical Review B **80**, 155406 (2009).
[7] M. S. Jang, H. Kim, Y.-W. Son, H. A. Atwater, and W. A. Goddard, Proceedings of the National Academy of Sciences **110**, 8786 (2013).
[8] Q. Wilmart, S. Berrada, D. Torrin, V. H. Nguyen, G. Fève, J.-M. Berroir, P. Dollfus, and B. Plaçais, 2D Materials **1**, 011006 (2014).

[9] K. S. Novoselov, E. McCann, S. Morozov, V. I. Falko, M. Katsnelson, U. Zeitler, D. Jiang, F. Schedin, and A. Geim, Nature physics **2**, 177 (2006).
[10] Y. Zhang, Y.-W. Tan, H. L. Stormer, and P. Kim, nature **438**, 201 (2005).
[11] T. Ohta, A. Bostwick, T. Seyller, K. Horn, and E. Rotenberg, Science **313**, 951 (2006).
[12] V. V. Cheianov and V. I. Falko, Physical review b **74**, 041403 (2006).
[13] A. V. Shytov, M. S. Rudner, and L. S. Levitov, Physical review letters **101**, 156804 (2008).
[14] E. Sonin, Physical Review B **79**, 195438 (2009).
[15] S. Chen, Z. Han, M. M. Elahi, K. M. Habib, L. Wang, B. Wen, Y. Gao, T. Taniguchi, K. Watanabe, J. Hone, et al., Science **353**, 1522 (2016).
[16] J. Cayssol, B. Huard, and D. Goldhaber-Gordon, Physical Review B **79**, 075428 (2009).
[17] P. E. Allain and J.-N. Fuchs, The European Physical Journal B **83**, 301 (2011).
[18] V. T. Phong and J. F. Kong, arXiv preprint arXiv:1610.00201 (2016).
[19] V. V. Cheianov, V. Fal'ko, and B. Altshuler, Science **315**, 1252 (2007).
[20] D. Dahal and G. Gumbs, Journal of Physics and Chemistry of Solids **100**, 83 (2017).
[21] C. Beenakker, Physical review letters **97**, 067007 (2006).
[22] R. N. Sajjad and A. W. Ghosh, Applied Physics Letters **99**, 123101 (2011).
[23] M. M. Elahi, K. Masum Habib, K. Wang, G.-H. Lee, P. Kim, and A. W. Ghosh, Applied Physics Letters **114**, 013507 (2019).
[24] M. I. Katsnelson, K. S. Novoselov, and A. K. Geim, Nature Physics **2**, 620 (2006).
[25] M. I. Katsnelson, *Graphene: Carbon in Two Dimensions* (Cambridge University Press, 2012).
[26] V. Zalipaev, C. Linton, M. Croitoru, and A. Vagov, Physical Review B **91**, 085405 (2015).
[27] K. J. A. Reijnders, D. S. Minenkov, M. I. Katsnelson, and S. Y. Dobrokhotov, Annals of Physics **397**, 65 (2018).
[28] E. B. Choubabi, A. Jellal, and M. Mekkaoui, The European Physical Journal B **92**, 85 (2019).
[29] M. Titov, Europhysics Letters **79**, 17004 (2007).
[30] J. Bardarson, J. Tworzydlo, P. Brouwer, and C. Beenakker, Physical Review Letters **99**, 106801 (2007).
[31] P. Ostrovsky, I. Gornyi, and A. Mirlin, Physical Review Letters **105**, 036803 (2010).
[32] J. Tworzydło, C. Groth, and C. Beenakker, Physical Review B **78**, 235438 (2008).
[33] A. R. Hernández and C. H. Lewenkopf, Physical Review B **86**, 155439 (2012).
[34] G. Xu, X. Xu, B. Wu, J. Cao, and C. Zhang, Journal of Applied Physics **107**, 123718 (2010).
[35] T. Low, S. Hong, J. Appenzeller, S. Datta, and M. S. Lundstrom, IEEE Transactions on Electron Devices **56**, 1292 (2009).
[36] R. Logemann, K. Reijnders, T. Tudorovskiy, M. Katsnelson, and S. Yuan, Physical Review B **91**, 045420 (2015).
[37] N. Ghobadi and Y. Abdi, Current Applied Physics **13**, 1082 (2013).
[38] D. Huang, A. Singh, and D. Cardimona, Physics Letters A **259**, 488 (1999).
[39] A. Iurov, G. Gumbs, O. Roslyak, and D. Huang, Journal of Physics: Condensed Matter **24**, 015303 (2011).
[40] A. Iurov, G. Gumbs, O. Roslyak, and D. Huang, Journal of Physics: Condensed Matter **25**, 135502 (2013).
[41] S. Y. Zhou, G.-H. Gweon, A. Fedorov, d. First, PN, W. De Heer, D.-H. Lee, F. Guinea, A. C. Neto, and A. Lanzara, Nature materials **6**, 770 (2007).
[42] G. Giovannetti, P. A. Khomyakov, G. Brocks, P. J. Kelly, and J. Van Den Brink, Physical Review B **76**, 073103 (2007).
[43] R. Balog, B. Jørgensen, L. Nilsson, M. Andersen, E. Rienks, M. Bianchi, M. Fanetti, E. Lægsgaard, A. Baraldi, S. Lizzit, et al., Nature materials **9**, 315 (2010).
[44] O. Kibis, Physical Review B **81**, 165433 (2010).
[45] K. Kristinsson, O. V. Kibis, S. Morina, and I. A. Shelykh, Scientific reports **6**, 20082 (2016).
[46] N. Horing, A. Iurov, G. Gumbs, A. Politano, and G. Chiarello, *Low-dimensional and nanostructured materials and devices* (2016).
[47] A. Iurov, G. Gumbs, D. Huang, and V. Silkin, Physical Review B **93**, 035404 (2016).
[48] P. Pyatkovskiy, Journal of Physics: Condensed Matter **21**, 025506 (2008).
[49] A. Iurov, G. Gumbs, D. Huang, and L. Zhemchuzhna, Journal of Applied Physics **121**, 084306 (2017).
[50] V. Vargiamidis and P. Vasilopoulos, Applied Physics Letters **105**, 223105 (2014).
[51] D. Huang, G. Gumbs, and O. Roslyak, Physical Review B **83**, 115405 (2011).
[52] A. Iurov, G. Gumbs, and D. Huang, Physical Review B **98**, 075414 (2018).

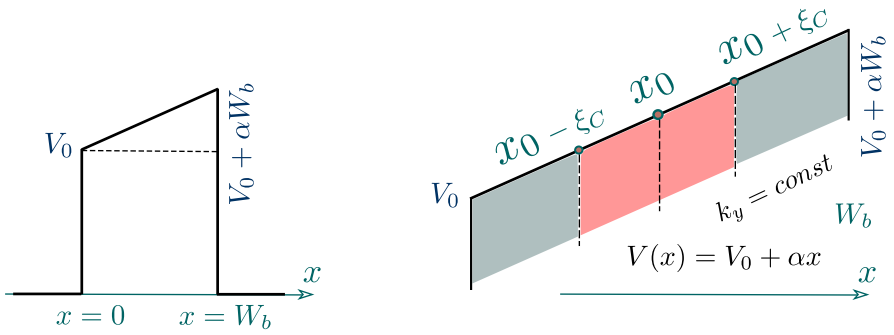

FIG. 1: (Color online) Schematics for the tilted barrier $V_B(x) = V_0 + \alpha x$ in the region of $0 \le x \le W_B$, as shown in the left panel, and two classical turning points at $x = x_0 \pm \xi_c$ in the right panel.

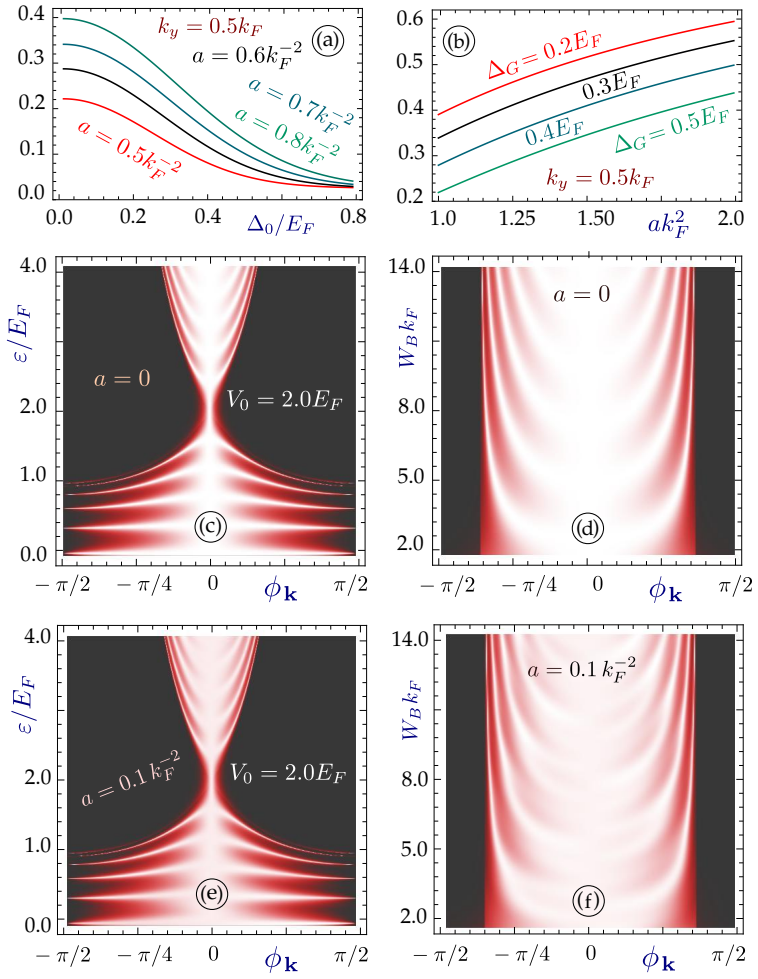

FIG. 2: (Color online) Transmission amplitude $T(\varepsilon, \phi_{\mathbf{k}})$ in graphene for fixed $V_0/E_F = 2$ and various barrier tilting parameters specified by different a values. Panels (a) and (b) display $T(\varepsilon, \phi_{\mathbf{k}})$ from Eq. (10) for gapped graphene as functions of Δ_G and ak_F^2, respectively, with fixed $k_y = 0.5\,k_F$. Panels (c)-(e) present density plots for $T(\varepsilon, \phi_{\mathbf{k}})$ from Eqs. (22) and (24) for gapless graphene $\Delta_G = 0$ as functions of ε/E_F and $\phi_{\mathbf{k}}$ in (c), (e) and functions of $W_B k_F$ and $\phi_{\mathbf{k}}$ in (d), (f) with $\varepsilon/E_F = 1$ for $a = 0$ (middle row) and for $a = 0.1\,k_F^{-2}$ (bottom row). Here, $V_0/E_F = 2$, $E_F = \hbar v_F k_F = 6.28\,\text{meV}$ is taken for the energy unit and k_F is the unit for wave number of electrons.

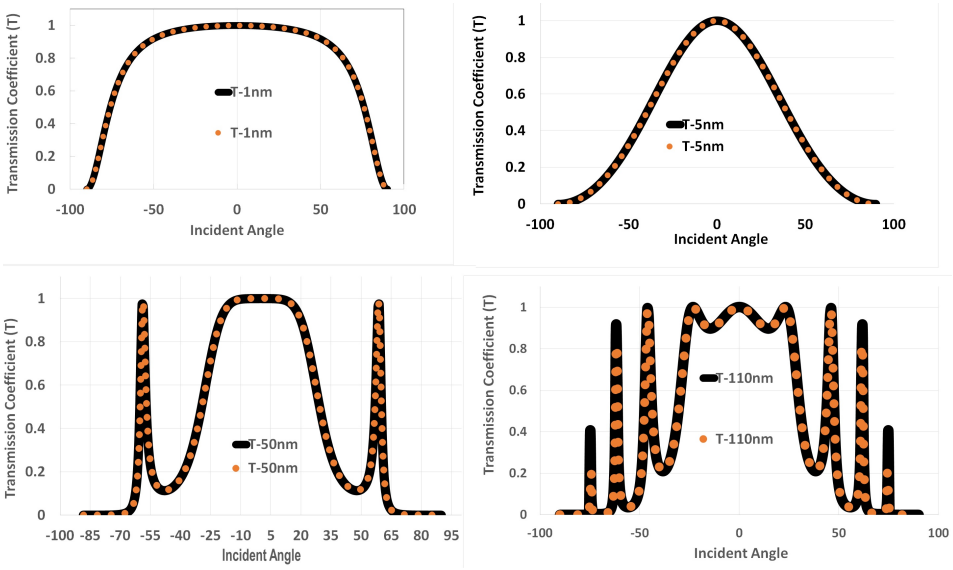

FIG. 3: (Color online) Comparison of calculated transmission coefficients $T(\varepsilon, \phi_{\mathbf{k}} \,|\, \mathcal{E}_0 = 0)$ with $V_d = 0$ as a function of incident angle $\phi_{\mathbf{k}}$ based on either an analytical solution (black-solid curves) or FDA (red-dotted curves) for four different barrier thickness $W_B = 1\,\text{nm}$ (upper-left), $5\,\text{nm}$ (upper-right), $50\,\text{nm}$ (lower-left) and $110\,\text{nm}$ (lower-right), where $V_0 = 285\,\text{meV}$, $\mathcal{E}_0 = 0$, and $\varepsilon = 80\,\text{meV}$ are chosen for calculations.

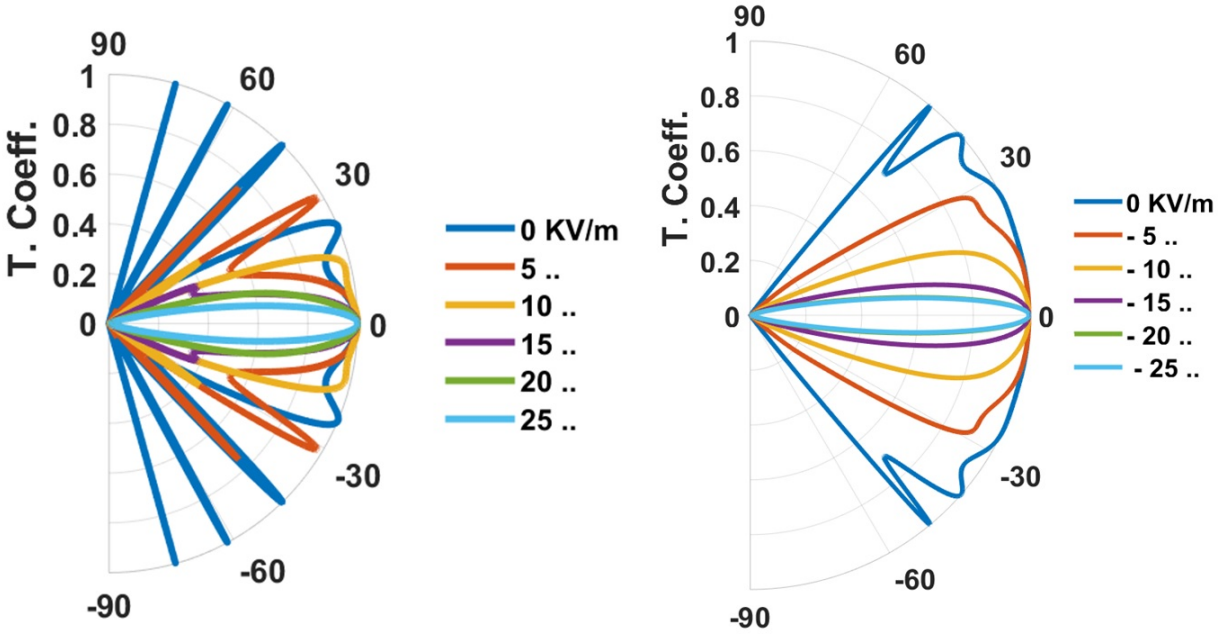

FIG. 4: (Color online) Polar plots for transmission coefficient $T(\varepsilon, \phi_{\mathbf{k}} \,|\, \mathcal{E}_0)$ as a function of incident angle $\phi_{\mathbf{k}}$ for different tilting fields $\mathcal{E}_0$, where both results for a reduced barrier $\mathcal{E}_0 > 0$ (left) and an enhanced barrier $\mathcal{E}_0 < 0$ (right) are shown in this figure for a full comparison. Here, $W_B = 110\,\text{nm}$, $V_0 = 285\,\text{meV}$, $\varepsilon = 80\,\text{meV}$ (left) and $400\,\text{meV}$ (right) are chosen.

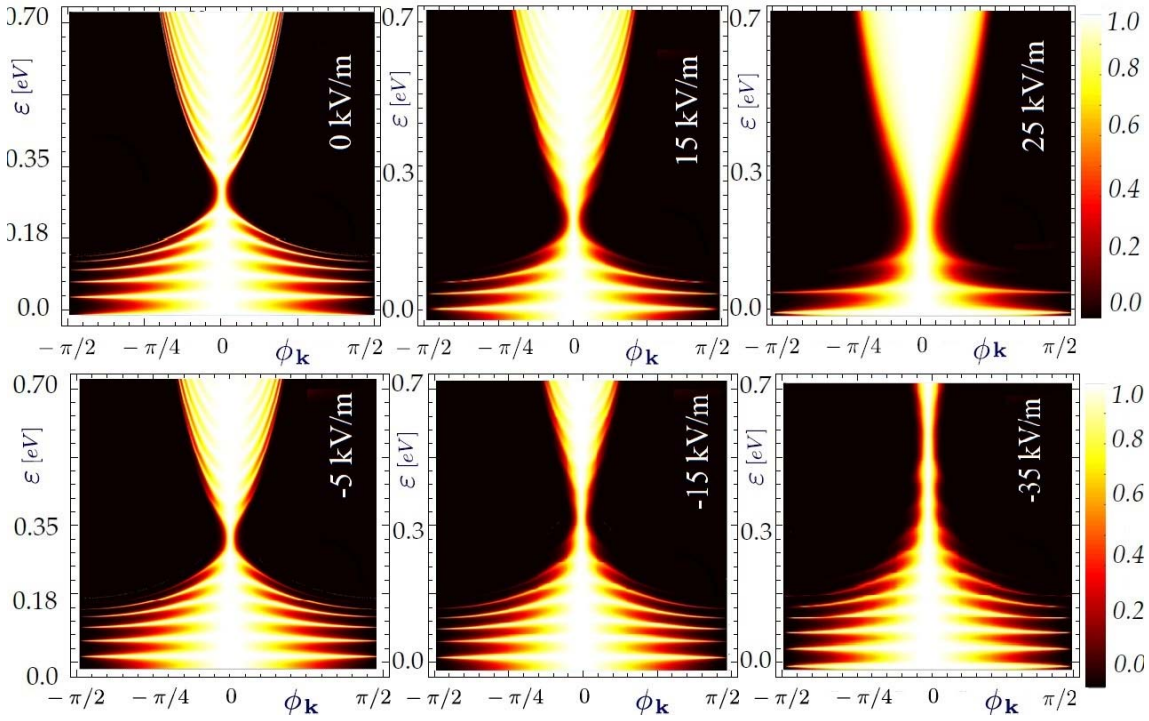

FIG. 5: (color online) Density plots of $T(\varepsilon, \phi_{\mathbf{k}} \,|\, \mathcal{E}_0)$ as functions of both ε and $\phi_{\mathbf{k}}$, where $W_B = 110\,\text{nm}$, $V_0 = 285\,\text{meV}$ and different values of $\mathcal{E}_0$ are assumed in various panels.

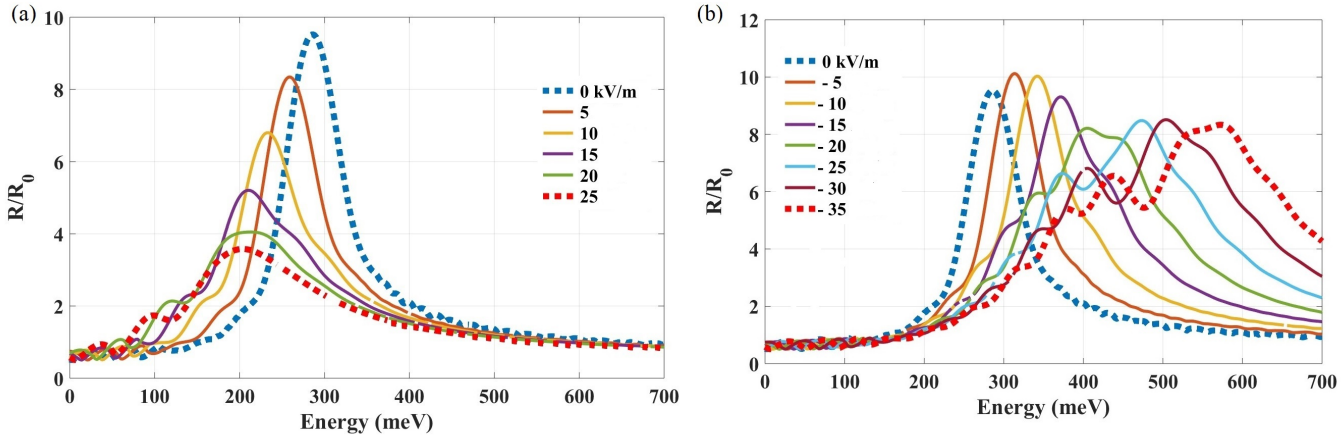

FIG. 6: (Color online) The ε dependence of the resistance ratio R/R_0 (inverse conductance) for coherent tunneling of Dirac electrons in graphene, calculated from Eq. (39), through a tilted barrier with different values for tilting fields $\mathcal{E}_0$. Here, R_0 is the resistance for normal incidence with $\phi_{\mathbf{k}} = 0$ and results for both reduced (left) and enhanced (right) barriers are presented for comparisons. Moreover, we set $W_B = 110\,\text{nm}$ and $V_0 = 285\,\text{meV}$ for calculations.

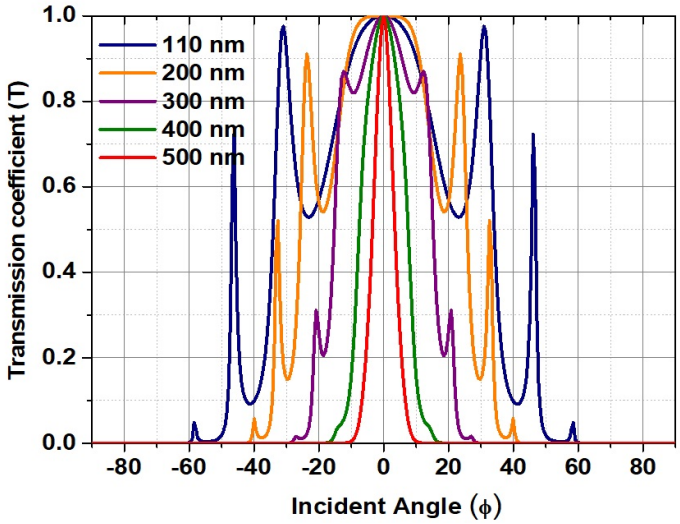

FIG. 7: (Color online) Transmission coefficient $T(\varepsilon, \phi_{\mathbf{k}} \,|\, \mathcal{E}_0)$ at $\mathcal{E}_0 = 5\,\mathrm{kV/m}$ as a function of incident angle $\phi_{\mathbf{k}}$ for various barrier widths $W_B = 110$ (black), 200 (orange), 300 (purple), 400 (green) and 500 nm (red), where $V_0 = 285\,\mathrm{meV}$ and $\varepsilon = 80\,\mathrm{meV}$.

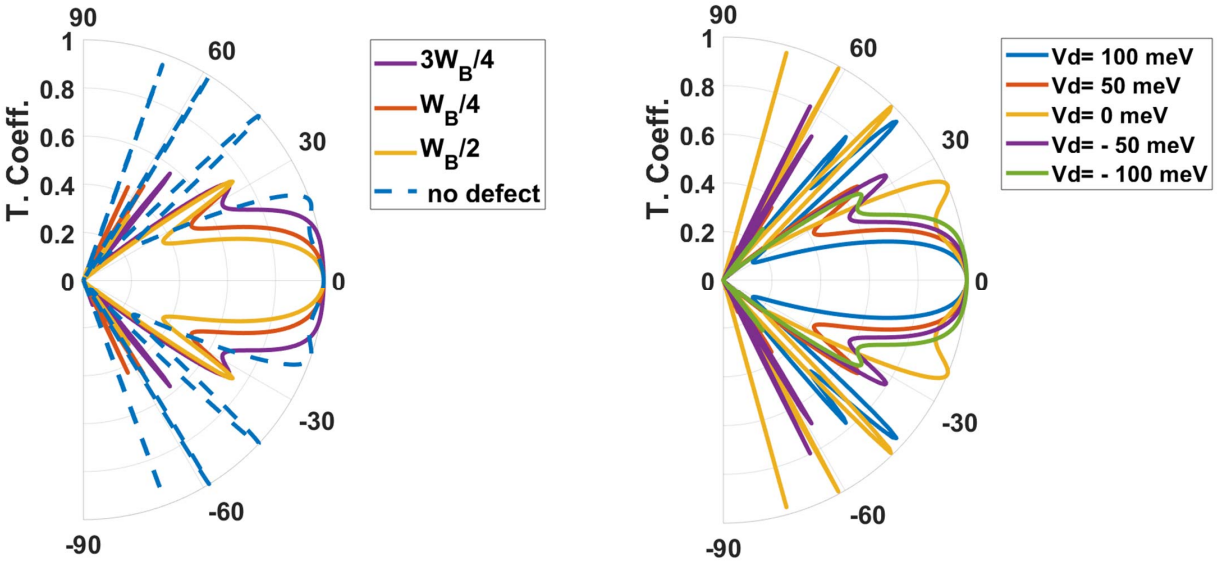

FIG. 8: (Color online) Polar plots for transmission coefficient $T(\varepsilon, \phi_{\mathbf{k}} \,|\, \mathcal{E}_0, V_d, x_s)$ with a single scatter as a function of incident angle $\phi_{\mathbf{k}}$ for different scattering positions x_s (left) and strengths V_d (right), where $W_B = 110\,\mathrm{nm}$, $V_0 = 285\,\mathrm{meV}$, $\varepsilon = 80\,\mathrm{meV}$, and $\mathcal{E}_0 = 0$ are chosen for calculations. Moreover, we also set $V_d = 50\,\mathrm{meV}$ in the left panel, while $x_s = W_B/2$ in the right panel.

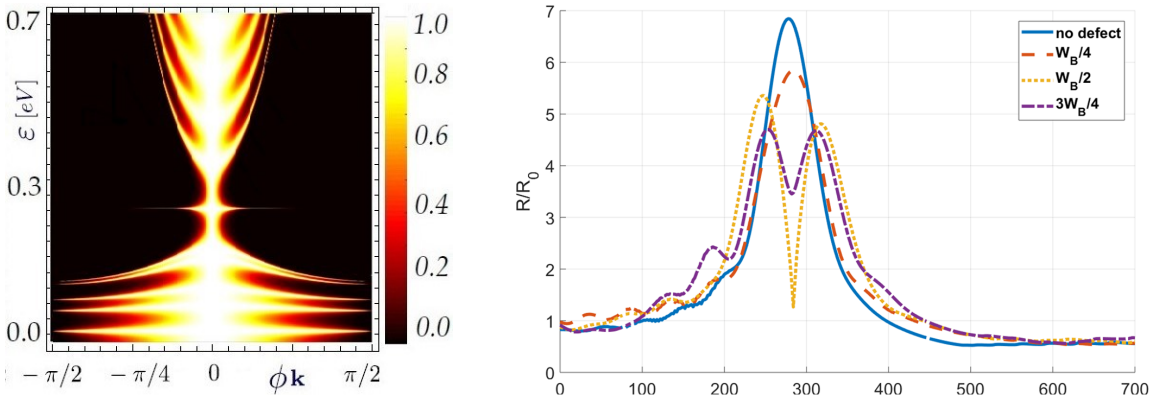

FIG. 9: (Color online) Density plots of $T(\varepsilon, \phi_{\mathbf{k}} \,|\, \mathcal{E}_0, V_d, x_s)$ as functions of both ε and $\phi_{\mathbf{k}}$ (left), as well as the ε dependence of the resistance ratio R/R_0 (right), for coherent tunneling of Dirac electrons in graphene through a square barrier embedded with a single scatter at different positions x_s. Here, we set $W_B = 110\,\text{nm}$, $V_0 = 285\,\text{meV}$, $\mathcal{E}_0 = 0$, and $V_d = 50\,\text{meV}$ for calculations. Moreover, we also set $x_s = W_B/2$ in the left panel.

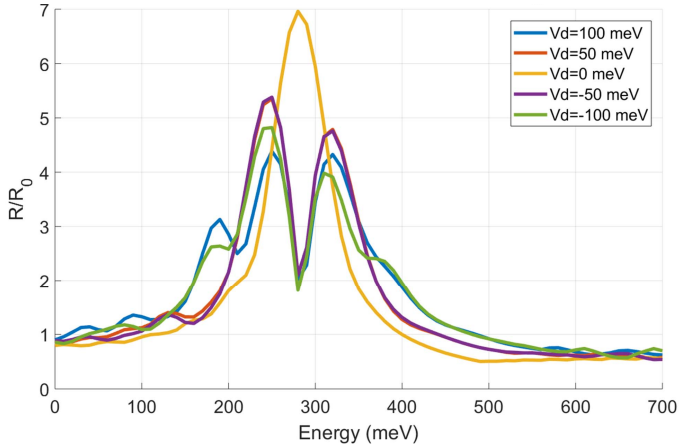

FIG. 10: (Color online) The ε dependence of the resistance ratio R/R_0 for coherent tunneling of Dirac electrons in graphene through a square barrier embedded with a single scatter having different strengths V_d. Here, we set $W_B = 110\,\text{nm}$, $V_0 = 285\,\text{meV}$, $\mathcal{E}_0 = 0$, and $x_s = W_B/2$ for calculations.

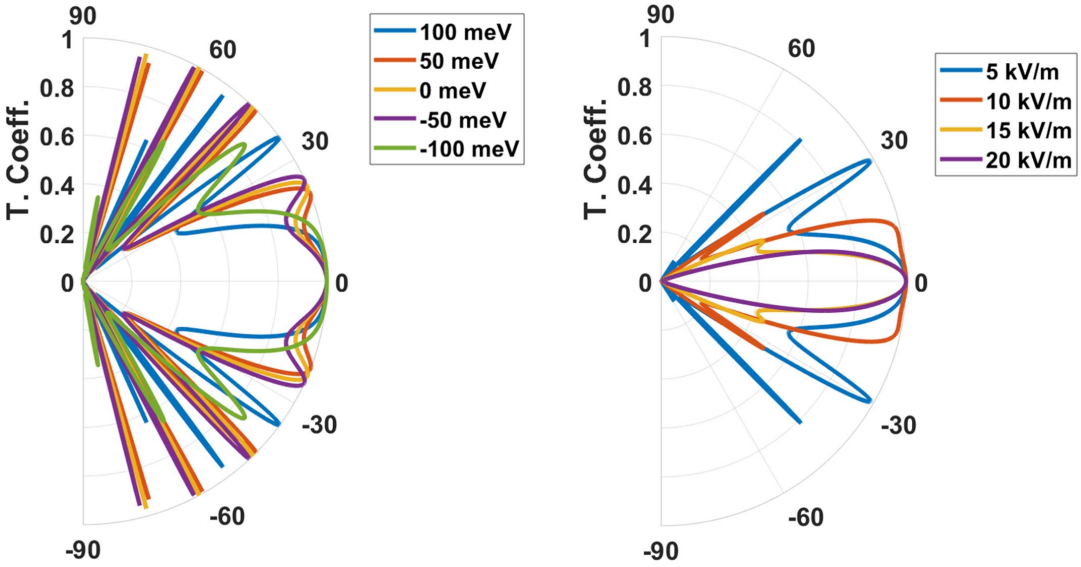

FIG. 11: (Color online) Polar plots for average transmission coefficient $\overline{T}(\varepsilon, \phi_{\mathbf{k}} \,|\, \mathcal{E}_0, V_d)$ having continuously-distributed scatters within a barrier as a function of incident angle $\phi_{\mathbf{k}}$, where $W_B = 110\,\text{nm}$, $V_0 = 285\,\text{meV}$ and $\varepsilon = 80\,\text{meV}$ are chosen for calculations. Moreover, in the left panel we assume $\mathcal{E}_0 = 0$ but set $V_d = 100$, 50, 0, -50 and $-100\,\text{meV}$, as indicated, for different scatter strengths. In the right panel, however, we have $V_d = 100\,\text{meV}$ while set $\mathcal{E}_0 = 5$, 10, 15 and $20\,\text{kV/m}$, as indicated, for various reduced barriers.

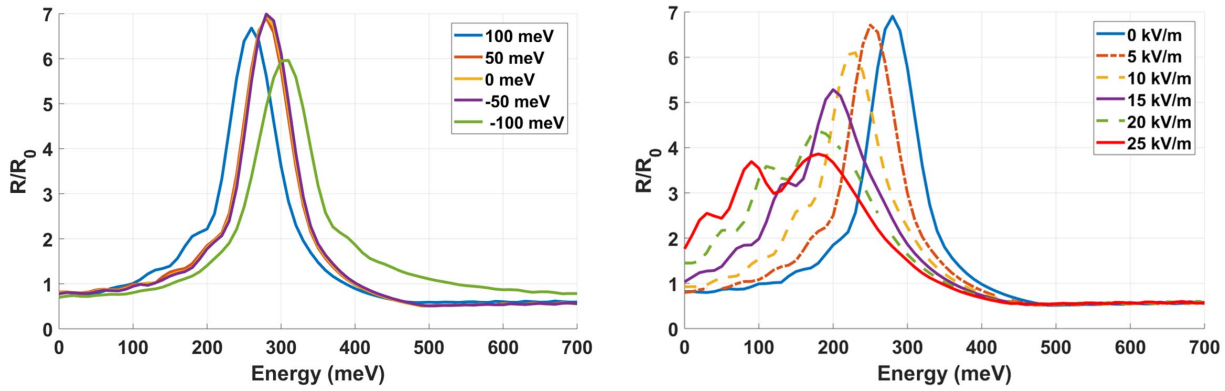

FIG. 12: (Color online) The ε dependence of the resistance ratio R/R_0 for incoherent tunneling of Dirac electrons in graphene through continuously-distributed scatters within a barrier, where $W_B = 110\,\text{nm}$ and $V_0 = 285\,\text{meV}$ are chosen for calculations. In the left panel, we have $\mathcal{E}_0 = 0$ while $V_d = 100$, 50, 0, -50 and $-100\,\text{meV}$, as indicated, for different scatter strengths. In the right panel, however, we set $V_d = 100\,\text{meV}$ but have $\mathcal{E}_0 = 0$, 5, 10, 15, 20, and $25\,\text{kV/m}$, as indicated, for various reduced barriers.